

Alma Mater Studiorum Università di Bologna  
Archivio istituzionale della ricerca

Lignin-derived bimetallic platinum group metal-free oxygen reduction reaction electrocatalysts for acid and alkaline fuel cells

This is the final peer-reviewed author's accepted manuscript (postprint) of the following publication:

*Published Version:*

Muhyuddin, M., Friedman, A., Poli, F., Petri, E., Honig, H., Basile, F., et al. (2023). Lignin-derived bimetallic platinum group metal-free oxygen reduction reaction electrocatalysts for acid and alkaline fuel cells. JOURNAL OF POWER SOURCES, 556, 1-12 [10.1016/j.jpowsour.2022.232416].

*Availability:*

This version is available at: <https://hdl.handle.net/11585/915070> since: 2024-09-11

*Published:*

DOI: <http://doi.org/10.1016/j.jpowsour.2022.232416>

*Terms of use:*

Some rights reserved. The terms and conditions for the reuse of this version of the manuscript are specified in the publishing policy. For all terms of use and more information see the publisher's website.

This item was downloaded from IRIS Università di Bologna (<https://cris.unibo.it/>).  
When citing, please refer to the published version.

(Article begins on next page)

17  
18 10 **Lignin-derived bimetallic platinum group metal-free oxygen reduction reaction**  
19 11 **electrocatalysts for acid and alkaline fuel cells**  
20 12

21 13 Mohsin Muhyuddin<sup>1</sup>, Ariel Friedman<sup>2</sup>, Federico Poli<sup>3</sup>, Elisabetta Petri<sup>3</sup>, Hilah Honig<sup>2</sup>, Francesco  
22 14 Basile<sup>4</sup>, Andrea Fasolini<sup>4</sup>, Roberto Lorenzi<sup>1</sup>, Enrico Berretti<sup>5</sup>, Marco Bellini<sup>5</sup>, Alessandro  
23 15 Lavacchi<sup>5</sup>, Lior Elbaz<sup>2</sup>, \*Carlo Santoro<sup>1</sup>, \*\*Francesca Soavi<sup>3</sup>  
24 16

25 17  
26 18 <sup>1</sup>Department of Materials Science, University of Milano-Bicocca, Via Cozzi 55, Building U5,  
27 19 20126 Milan, Italy

28 20 <sup>2</sup> Department of Chemistry and the Institute of Nanotechnology and Advanced Materials, Bar-Ilan  
29 21 University, Ramat-Gan 5290002, Israel

30 22 <sup>3</sup>Department of Chemistry “Giacomo Ciamician”, Alma Mater Studiorum – Università di  
31 23 Bologna, Italy

32 24 <sup>4</sup> Department of Industrial Chemistry “Toso Montanari”, Alma Mater Studiorum – Università di  
33 25 Bologna, Italy

34 26 <sup>5</sup> Istituto di Chimica Dei Composti OrganoMetallici (ICCOM), Consiglio Nazionale Delle  
35 27 Ricerche (CNR), Via Madonna Del Piano 10, 50019 Sesto Fiorentino, Firenze, Italy

36 28 \* Carlo Santoro: carlo.santoro@unimib.it

37 29 \*\* Francesca Soavi: francesca.soavi@unibo.it

38 30 **Abstract**

39 31 Metal-nitrogen-carbons (M-N-Cs) as a reliable substitution for platinum-group-metals (PGMs) for  
40 32 oxygen reduction reaction (ORR) are emerging candidates to rationalize the technology of fuel  
41 33 cells. The development of M-N-Cs can further be economized by consuming waste biomass as an  
42 34 inexpensive carbon source for the electrocatalyst support. Herein, we report the simple fabrication  
43 35 and in-depth characterization of electrocatalysts using lignin-derived activated char. The activated  
44 36 char (LAC) was functionalized with phthalocyanine (FePc and MnPc) via atmosphere-controlled  
45 37 pyrolysis to produce monometallic M-N-Cs (L\_Mn and L\_Fe) and bimetallic M1-M2-N-Cs  
46 38 (L\_FeMn) electrocatalysts. Raman spectroscopy and transmission electron microscopy (TEM)  
47 39 revealed a defect-rich architecture. XPS confirmed the coexistence of various nitrogen-containing  
48 40 active moieties. L\_Fe and L\_FeMn demonstrated appreciable ORR in both acidic and alkaline  
49 41 conditions whereas L\_FeMn helped in restricting the peroxide yield, particularly in alkaline media.  
50 42 L\_Fe and L\_FeMn demonstrated remarkable onset potential ( $E_{\text{onset}}$ ) of  $\sim 0.942\text{V}$  (vs RHE) with an  
51 43  $E_{1/2}$  of  $0.874\text{V}$  (vs RHE) in  $0.1\text{M KOH}$ . In acid, L\_FeMn had an  $E_{\text{onset}}$  of  $0.817\text{V}$  (vs RHE) and an

1  
2  
3  
4 1  $E_{1/2}$  of  $\sim 0.76\text{V}$  (vs RHE). Finally, the L\_FeMn cathode electrocatalyst was integrated and tested in  
5  
6 2 PEMFC and AEMFC. AEMFC demonstrated optimistic performance with a peak power density  
7  
8 3 of  $261\text{ mW cm}^{-2}$  at the current density of  $\sim 577\text{ mA cm}^{-2}$ .  
9

10 4  
11 5 **Keywords:** lignin-derived char, oxygen reduction reaction, platinum group metal-free, proton  
12 6 exchange membrane fuel cell, anion exchange membrane fuel cell  
13  
14  
15 7

## 16 8 **1. Introduction**

19 9 Low-temperature fuel cells (FCs) being capable of converting chemical energy into electrical  
20  
21 10 energy without contributing to planetary carbon footprints are one of the most paramount  
22  
23 11 candidates to sustainably address the global energy crises. Within the paradigm of advanced FCs,  
24  
25 12 analogous technologies of proton exchange membrane FCs (PEMFCs) and anion-exchange-  
26  
27 13 membrane FCs (AEMFCs) are capturing scientific attention owing to their unique merits. Both  
28  
29 14 technologies with different pH of electrolytic media realize the incessant translation of energy  
30  
31 15 through hydrogen oxidation reaction (HOR) at the anode and the oxygen reduction reaction (ORR)  
32  
33 16 at the cathode, leaving water as a green byproduct. However, even though FCs are having  
34  
35 17 considerable commercial success, the complex and lethargic ORR constitutes the key hindrance in  
36  
37 18 their practical deployment on a large scale since it is several orders of magnitude slower than the  
38  
39 19 HOR [1–3]. Reduction of oxygen follows multielectron transfer routes with sluggish kinetics,  
40  
41 20 imposing much higher overpotential and thus restricting the overall device efficiency. It is known  
42  
43 21 in the scientific community that ORR usually proceeds either in a bi-electronic or tetra-electronic  
44  
45 22 fashion producing peroxide or water, respectively [4–8]. From the perspective of FCs, the tetra-  
46  
47 23 electronic pathway is essentially important whereas the production of highly reactive peroxide  
48  
49 24 during bi-electronic ORR not only makes the system less energy efficient but also severely affects  
50  
51 25 the integrity of membrane electrode assembly (MEA) and stack architecture. To deal with the  
52  
53 26 aforementioned challenges, platinum group metals (PGMs) are typically employed which  
54  
55 27 eventually make the application of FCs economically impracticable. The use of scarce and  
56  
57 28 expensive Pt in the fabrication of ORR electrocatalysts accounts for more than 55% of the total  
58  
59 29 cost of an FC stack [9,10]. Moreover, state-of-the-art Pt-based electrocatalysts are also notorious  
60  
61 30 for their undesired dissolution, nanoparticle coalescence and poisoning with common  
62  
63 31 contaminants which in turn gravely diminish the electrocatalytic efficiency [10,11]. Therefore, it  
64  
65

1 is an urgent need of the hour to cope with such complications either by reducing the Pt content or  
2 by substituting with PGM-free electrocatalysts. In the pursuit of PGM-free electrocatalysis, metal-  
3 nitrogen-carbons (M-N-Cs, M=Mn, Fe, Co, Ni etc.) are emerging as a reliable competitor in which  
4 earth-abundant transition metals (TM) having coordination with different nitrogen species ( $MN_x$ )  
5 make active moieties for ORR within the porous carbonaceous framework [6,12–17].

6 In the search for an efficacious M-N-C electrocatalyst, various designing parameters must  
7 be considered. First comes the porous nature of carbonaceous architecture. Carbon provides a  
8 conducive platform for the whole electrochemical activity whereas a high surface area and  
9 mesoporous environment boost the mass transport of gaseous reagents to the active sites [18].  
10 Where the intrinsic defects, ruptured facets and structural discontinuities in carbon facilitate the  
11 binding of oxygen [19], the dangling bonds present in the unsaturated vacancies also contribute to  
12 the doping of secondary elements i.e. nitrogen to generate the active moieties [20]. Furthermore,  
13 nitrogen doping breaks the electro-neutrality of the carbon triggering the chemisorption of  $O_2$  [21]  
14 and due to enhanced Lewis basicity, pyridinic-nitrogen effectively participates in ORR by  
15 subsequently reducing the peroxide intermediate into water [22,23]. Over and above that, the  
16 selection of the transition metal is a strategic task in electrocatalyst development as the electrons  
17 transfer from metal to oxygen is primarily dictated by the redox potential of the central metal  
18 [16,24–26] and hence the plurality of redox sites is one of the foremost prerequisites for  $O_2$   
19 activation and the subsequent reduction [16].  $MN_x$  ( $x=2,3,4$ ) is undoubtedly the most  
20 electrocatalytically active site in which a central TM atom has coordination with pyridinic nitrogen  
21 ligands on the distorted carbon surface and aptly bio-mimic the natural enzyme to reduce oxygen  
22 [27–30]. In addition to the conventional exploitation of metal salts and organic precursors of  
23 nitrogen and carbon for the fabrication of M-N-Cs, the use of metal macrocyclic compounds i.e.  
24 metal phthalocyanine (MPc) and porphyrins have the preferred  $MN_4$  sites. However, a  
25 thermomechanical treatment known as pyrolysis becomes inevitably imperative to achieve the  
26 mandatory durability and robustness. This occurs by integrating the  $MN_4$  active site onto the  
27 carbon backbone, favored by the high-temperature treatment. Although such active sites can be  
28 generated using MPc of different first-row TM, Fe- $N_4$  finds its place at the apex of the volcano  
29 curve due to its moderate adsorption portfolio [13,16,24,25,31]. It is noteworthy that FePc and  
30 MnPc promote the tetra-electronic ORR by rupturing the O-O bond due to the preferable 'd

1  
2  
3  
4 1 *character*'. On the other hand, it was shown that CoPc, NiPc and CuPc tend to catalyze the ORR  
5  
6 2 in a bi-electronic manner, underlined by the high intermediate production measured [16,24,31,32].

7  
8 3 Notwithstanding the fact that Fe-N-Cs are glossing in the arena of PGM-free  
9  
10 4 electrocatalysis, their performance is still inferior compared to PGM-based electrocatalysts,  
11  
12 5 spurring extensive global ventures to understand and improve the activity of Fe-N-Cs [33–39]. To  
13  
14 6 mitigate the efficiency pitfalls, the introduction of a second TM could be useful [40]. Serov et al.  
15  
16 7 analyzed the influence of Fe interaction with a second TM by developing a series of  
17  
18 8 electrocatalysts using a sacrificial support method (SSM) and observed a substantial upturn in  
19  
20 9 ORR activity after the addition of a second TM [41]. At the present, some acknowledgeable efforts  
21  
22 10 have been made to co-doped Fe and Co [42–46]. However, again the usage of Co challenges the  
23  
24 11 economic rationalization of FCs since it is listed among critical raw materials[47,48] and also Co  
25  
26 12 holds the tendency of producing higher peroxide [17,49]. Moreover, as compared to Co, the  
27  
28 13 supplementation of Mn into Fe-carrying M-N-Cs clearly improves the electrocatalytic activity by  
29  
30 14 keeping the peroxide generation relatively lower which ultimately hastens up the cathodic  
31  
32 15 performance [50–52].

33  
34 16 In parallel, a growing scientific interest has recently been witnessed in the development of  
35  
36 17 ORR electrocatalysts using waste biomasses [53–59] and plastics [60–64] as a cheaper and readily  
37  
38 18 available source of carbon and such initiatives could circularly ensure ecological safety. Global  
39  
40 19 agricultural waste generation is gigantically increasing on annual basis [65] and hence, its  
41  
42 20 transformation into innovative materials is rationally justified considering the environmental gains  
43  
44 21 of waste reduction [53]. As already mentioned, porosity and high surface area are primarily  
45  
46 22 required for providing accessibility to the active sites, biomasses owing to trimodal structures  
47  
48 23 efficiently fulfill this prerequisite and act as a tailorable pattern for novel materials  
49  
50 24 fabrication[55,66]. Among these biomass wastes, lignin derived from waste biomass is one of the  
51  
52 25 most produced agricultural wastes. According to an estimation, annual global harvesting of  
53  
54 26 biomass accounts for more than 170 billion metric tons [67] out of which lignin is present up to  
55  
56 27 25% [68] whereas the pulp and paper industry generates up to 50-70 million tons per year [69,70]  
57  
58 28 which is expected to surpass the figure of 225 million tons annually by the year 2030 [70,71].

59  
60 29 Herein, within the core of the circular economy, we valorize real waste lignin and transform  
61  
62 30 it through pyrolysis and activation processes into high surface area char that is then functionalized  
63  
64 31 with mono- and bi-metallic phthalocyanine and tested as PGM-free electrocatalyst for oxygen  
65

1  
2  
3  
4 1 reduction reaction in acid and alkaline media. After a complete physio-chemical and  
5  
6 2 electrochemical characterization, the lignin-derived PGM-free electrocatalysts are integrated into  
7  
8 3 cathode electrodes and tested in PEMFC and AEMFC.  
9

## 10 4 11 5 **2. Materials and Methods**

### 12 13 6 **2.1. Lignin Derived Activated Char (LAC)**

14  
15 7 Lignin-derived Activated Char (LAC) was produced by adapting the process reported in ref [59].  
16  
17 8 The raw lignin, a real solid waste of an anaerobic biodigester plant located in Bologna (Biotec Sys  
18  
19 9 srl), was washed with a water/ethanol mixture and then dispersed in an aqueous solution with a  
20  
21 10 mild activating agent,  $\text{KHCO}_3$  for 24 h (1:2 of Lignin: $\text{KHCO}_3$  in ratio). The dried mold was kept  
22  
23 11 in two identical grids, placed in a Tubular Oven (ELITE TSH16/50/610-2216E) and pyrolyzed  
24  
25 12 under  $\text{N}_2$  flux by heating from room temperature to  $850^\circ\text{C}$  and held for 1 h while keeping the  
26  
27 13 heating and then left to cool down. The biochar resulting from the two grids was mixed and sieved  
28  
29 14 before proceeding with a deashing with 3 M HCl for 8 h and washing with deionized water under  
30  
31 15 a vacuum. In the end, soxhlet extraction with water was performed. The activated char (LAC)  
32  
33 16 produced featured a specific surface area of  $1367 \text{ m}^2 \text{ g}^{-1}$ .

### 34 35 18 **2.2. Electrocatalyst Synthesis**

36  
37 19 The synthesis of electrocatalysts was carried out by functionalizing the (LAC) with the metal(s)-  
38  
39 20 phthalocyanine (MPc) of interest. To begin with, 80 wt.% of LAC was thoroughly mixed with 20  
40  
41 21 wt.% MPc. **Table 1** demonstrates the weight proportions of LAC and MPc set to fabricate  
42  
43 22 monometallic and bimetallic samples. The homogenized mixture obtained in the first step was then  
44  
45 23 transferred into a clean ceramic boat and subjected to a controlled atmosphere tube furnace  
46  
47 24 (Carbolite) for high-temperature pyrolysis. During the pyrolysis, the material was taken from room  
48  
49 25 temperature to  $600^\circ\text{C}$  and held there for 1 h while keeping the heating and cooling ramp rates at  
50  
51 26  $5^\circ\text{C min}^{-1}$ . Whereas the whole process was performed in 5 wt.%  $\text{H}_2$  balanced with  $\text{N}_2$  at  $100 \text{ cm}^3$   
52  
53 27  $\text{min}^{-1}$ . Afterward, the obtained electrocatalyst was rigorously homogenized by giving a round of  
54  
55 28 ball milling ( $E_{\text{MAX}}$ , Retsch GmbH, Germany) at 400 rpm for 40 min using zirconia balls of 3 mm  
56  
57 29 diameter.  
58  
59 30  
60  
61  
62  
63  
64  
65

1  
2  
3  
4 1 **Table 1.** Description of the samples studied.  
5

Sample Names	LAC (Wt. %)	FePc (Wt. %)	MnPc (Wt. %)
LAC	100	--	--
L_Fe	80	20	--
L_Mn	80	--	20
L_FeMn	80	10	10

17 2  
18  
19 3 **2.3. Structural and Morphological Characterization**

20  
21 4 The textural properties of the LAC were evaluated by nitrogen adsorption porosimetry  
22  
23 5 measurements that were carried out at 77 K with an ASAP 2020 system (Micromeritics) after a  
24  
25 6 drying step for 24 h at 413 K. The Brunauer-Emmett-Teller (BET) and density functional (DFT)  
26  
27 7 theories were used to analyze N<sub>2</sub> adsorption isotherm, in order to obtain specific surface area (S<sub>BET</sub>)  
28  
29 8 and pores size distribution (PSD), respectively.

30 9 Thermogravimetry analysis (TGA) was conducted using TA Instrument TGA Q50  
31  
32 10 analyzer in the oxygen atmosphere, in order to evaluate the ash content of the LAC produced. The  
33  
34 11 analysis was performed by applying a temperature ramp of 10°C/min from RT to 850°C.

35 12 Energy-dispersive X-ray fluorescence (XRF) having an X-ray tube with a molybdenum anode  
36  
37 13 (Bruker Artax 200 spectrometer) was utilized to perform qualitative elemental analysis. For the  
38  
39 14 crystal structure evaluation, X-ray diffraction (XRD, Rigaku Miniflex 600) with a copper source  
40  
41 15 was employed in the 2θ range of 10-90°. To investigate the carbonaceous structure of as-developed  
42  
43 16 electrocatalysts, Raman spectroscopy (LabRam, Jobin Yvon, France) was utilized where helium-  
44  
45 17 neon laser (λ=632.8 nm) as an excitation source was focused on the sample with the help of BX40  
46  
47 18 microscope (Olympus, Japan) while a silicon-based CCD system (Sincerity, Jobin Yvon, France)  
48  
49 19 was used to collect the signals.

50 20 X-ray photoelectron spectroscopy (XPS) was carried out using a Nexsa spectrometer  
51  
52 21 (England) equipped with a monochromatic, micro-focused, lower Al Ka X-ray (photon energy  
53  
54 22 1486.6 eV). Survey and high-resolution spectra were acquired at pass energy of 200 eV and 50  
55  
56 23 eV, respectively. The source power was normally 72W. All elements' binding energies were  
57  
58 24 recalibrated by setting the CC/CH component of the adventitious carbon 1st peak at 285 eV. The  
59  
60 25 measurements were carried out under UHV conditions, at a base pressure of 5x10<sup>-10</sup> torr (and no  
61  
62  
63  
64  
65

higher than  $3 \times 10^{-9}$  torr). Data analysis was performed using AVANTAGE software. Linear background subtraction was used for all spectra. High-Resolution Transmission electron microscopy (HRTEM) measurements were done using, JEOL JEM 2100, LaB6 filament, 200 kV.

## 2.4. Electrochemical Analysis

The kinetic parameters of the developed electrocatalysts were investigated through the rotating ring disk electrode (RRDE) methodology (Pine WaveVortex RDE connected with a Pine bipotentiostat). For the preparation of inks, 5 mg of the synthesized electrocatalyst was suspended in a solution containing 985  $\mu\text{L}$  of isopropanol (Alfa Aesar) and 15  $\mu\text{L}$  of 5 wt.% Nafion<sup>®</sup> D-520 (Alfa Aesar). The inks were homogenized by probe sonication for 10 mins followed by ultrasonic bath sonication for the next 30 mins at ambient temperature. E6R2 series RRDE electrode was used to fabricate the working electrode with  $0.2 \text{ mg cm}^{-2}$  and  $0.6 \text{ mg cm}^{-2}$  loadings of each electrocatalyst. In-house prepared 0.5 M  $\text{H}_2\text{SO}_4$  and 0.1 M KOH solutions were used as the electrolytic media in  $\text{O}_2$ -saturated circumstances to simulate ORR activity in acidic and alkaline conditions, respectively. The experiments were run in a three-electrode configuration encompassing a Pt-based counter electrode, saturated calomel electrode (SCE) as a reference and RRDE working electrode while 85% IR compensations were made using SP-100 Biologic<sup>®</sup> potentiostat. In this study, all the potentials are presented with respect to reversible hydrogen potential (RHE) after adding a factor of  $0.241 + \text{pH} \times 0.0591$  into the measured potentials which were originally referenced to SCE. Linear sweep voltammetry (LSV) was executed to acquire polarization curves at  $5 \text{ mV s}^{-1}$  between 1200 and 0 mV vs RHE while maintaining the ring potential  $\sim 1200 \text{ mV vs RHE}$ . ORR measurements were performed by rotating the RRDE at 1600 rpm. Before getting the actual LSV curves, the electrocatalyst was conditioned with multiple cyclic voltammograms until a stable current was achieved. The peroxide yield and number of electron transfers ( $n$ ) during ORR were estimated by monitoring the disk current ( $I_{\text{disk}}$ ) and ring current ( $I_{\text{ring}}$ ) using the following equations:

$$\text{Peroxide (\%)} = \frac{200 \times \frac{I_{\text{ring}}}{N}}{I_{\text{disk}} + \frac{I_{\text{ring}}}{N}} \quad (\text{eq.1})$$

$$n = \frac{4 I_{\text{disk}}}{I_{\text{disk}} + \frac{I_{\text{ring}}}{N}} \quad (\text{eq.2})$$



1  
2  
3  
4 1 The electrochemical stability was analyzed by applying 5000 cycles in the potential range between  
5  
6 2 1100 and 300 mV vs RHE at  $50 \text{ mV s}^{-1}$  in the  $\text{O}_2$ -saturated electrolytes by rotating the RRDE (with  
7  
8 3  $0.6 \text{ mg cm}^{-2}$  electrocatalyst loading) at 1600 rpm. For making a comparison, ORR polarization  
9  
10 4 curves were obtained again at  $5 \text{ mV s}^{-1}$ .  
11  
12 5

## 13 6 **2.5. Fuel Cell Fabrication and Testing**

### 14 15 16 7 **2.5.1 AEMFC**

17  
18 8 All AEMFC electrodes used in this work were prepared as described in detail in our previous  
19  
20 9 publications [72,73]. In brief, the electrocatalyst powder (80% wt.) was mixed with the ETFE-  
21  
22 10 based anion exchange ionomer powder (20% wt.) containing benzyl trimethylammonium (BTMA)  
23  
24 11 functional groups in 10 ml of distilled water and 2 propyl alcohol (1:1) solution. The resulting ink  
25  
26 12 was homogenized by 30 mins of ultrasound treatment (45 kHz, 100 W) and then sprayed using an  
27  
28 13 Iwata<sup>®</sup> spray gun onto the gas diffusion layer TGP-H-60 carbon paper 10% PTFE purchased by  
29  
30 14 Alfa Aesar. The catalyst spray was suspended every once in a while to dry the electrode for 10 sec  
31  
32 15 on an  $80 \text{ }^\circ\text{C}$  hot plate and subsequently weighed to control the electrocatalyst correct loading. The  
33  
34 16 anode loading was ca.  $0.4 \text{ mg}_{\text{PtRu}} \text{ cm}^{-2}$ , the cathode coating was  $0.8 \text{ mg}_{\text{electrocatalyst}} \text{ cm}^{-2}$ .

35  
36 17 The anion exchange membrane (AEM) preparation procedure has previously been  
37  
38 18 described in ref. [74] and consists of a  $10 \text{ }\mu\text{M}$  HDPE sheet functionalized with vinylbenzyl chloride  
39  
40 19 monomer by electron-beam radiation grafting ( $100 \text{ kGy}$  absorbed dose). The membrane was  
41  
42 20 subjected to amination treatment with aqueous TMA (45 wt %). The AEM and the electrodes were  
43  
44 21 immersed in  $1 \text{ M}$  KOH aqueous solution for 1 h before assembly into a  $5 \text{ cm}^2$  fuel cell fixture  
45  
46 22 (Scribner Associates) using a  $5 \text{ N m}$  torque. The AEMFC was tested with a Scribner Associates  
47  
48 23 850e fuel cell test station setting the cell temperature at  $60 \text{ }^\circ\text{C}$ . The anode was fed with pure  
49  
50 24 hydrogen at  $54 \text{ }^\circ\text{C}$  (75% relative humidity) at  $0.3 \text{ L min}^{-1}$  flow rate and the cathode was fed with  
51  
52 25 pure oxygen at  $60 \text{ }^\circ\text{C}$  (100% relative humidity) at  $0.6 \text{ L min}^{-1}$ . The cell was characterized by  
53  
54 26 consecutive 20 scan voltage experiments from OCV to  $0.3 \text{ V}$  applying a  $10 \text{ mV s}^{-1}$  linear sweep.  
55  
56 27

### 57 58 59 60 28 **2.5.2 PEMFC**

61  
62  
63  
64  
65 29 The electrocatalyst (L\_FeMn) was also tested in a PEM-FC. 152 mg of Nafion solution (D1021),  
66  
67 30 0.566 mL of isopropanol and 0.477 mL of water were added to 26 mg of the electrocatalyst. The  
68  
69 31 ink was sonicated for 1.5 h in ice. The electrocatalyst was sprayed on the 29BC gas diffusion layer

(GDL) using the airbrush. The final loading was  $\sim 4.4 \text{ mg cm}^{-2}$ . A commercial gas diffusion electrode (GDE) (Fuel Cells Etc., CST-GDE-01) of  $0.2 \text{ mg cm}^{-2}$  of Pt/C was used at the anode side. The anode GDE was hot pressed with NR-211 Nafion membrane ( $130 \text{ }^\circ\text{C}$ ) for 5 min. Then, the cathode GDE was assembled without hot pressing the MEA. The cell was tightened up to 10 Nm.

The cell was operated at  $80 \text{ }^\circ\text{C}$ . For testing the MEA, hydrogen ( $0.5 \text{ L min}^{-1}$ ) and air ( $0.7 \text{ L min}^{-1}$ ) were used at the anode and cathode sides, respectively (both at  $80 \text{ }^\circ\text{C}$ ). Break-in was performed by holding the cell at  $0.15 \text{ mA cm}^{-2}$  until the cell voltage was stabilized ( $\sim 5 \text{ min}$ ). Then, the voltage was scanned between 0.0 to 0.7 V ( $0.025 \text{ A/point}$ , 30 sec) and from 0.7 V to 0.2 V ( $0.05 \text{ A/point}$ , 30 sec).

### 3. Results and Discussion

#### 3.1. Initial Characterization of lignin Derived Activated Char

Black char was formed after the pyrolysis of the waste lignin. Importantly, initial screening evaluating the BET surface area ( $S_{\text{BET}}$ ) and the ash content was conducted.

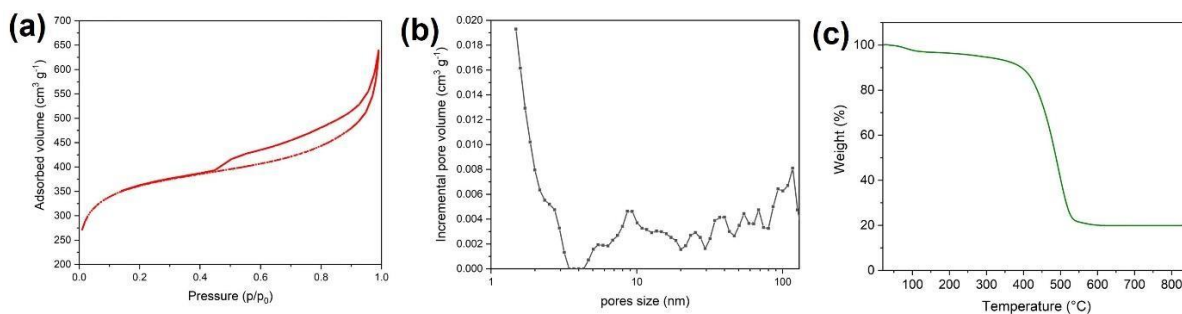


**Figure 1.** N<sub>2</sub> adsorption-desorption isotherms (a), pore size distribution (b) and thermogravimetric analysis (c) of LAC.

The evaluation of the surface area and pore size distribution was carried out by analyzing the N<sub>2</sub> adsorption/desorption isotherms at 77 K which is reported in Figure 1a. At low pressures, the isotherm branch of the LAC sample illustrated sharp adsorption inflection which is indicative of type I and materials containing micropores. However, at higher relative pressures of  $0.45 < P/P_0 < 1.0$ , the presence of an H4 hysteresis loop indicates that LAC is a complex material containing interconnected micropores and mesopores (type IV).

1 These observations are confirmed by the DFT pore size distribution that is reported in terms of  
 2 incremental pore volume in Figure 1b. The micropore volume ( $V_{\text{micro}}$ ), mesopore volume ( $V_{\text{meso}}$ )  
 3 and total pore volume ( $V_{\text{total}}$ ) of the sample is charted in Table 2 along with the BET surface area  
 4 ( $S_{\text{BET}}$ ). The  $S_{\text{BET}}$  is  $1367 \pm 1 \text{ m}^2 \text{ g}^{-1}$ . Such high value is mainly related to micropores and small  
 5 mesopores ( $< 3\text{nm}$ ). Indeed,  $V_{\text{micro}}$  ( $0.40 \text{ cm}^3 \text{ g}^{-1}$ ) accounts for the 70%  $V_{\text{total}}$  ( $0.57 \text{ cm}^3 \text{ g}^{-1}$ ). Larger  
 6 pores are almost equally distributed from 3 nm up to more than 100 nm, and contribute with only  
 7 the 20% to  $V_{\text{total}}$  ( $V_{\text{meso}} = 0.12 \text{ cm}^3 \text{ g}^{-1}$ ).

8  
 9 **Table 2.** DFT micropore volume ( $V_{\text{micro}}$ ), mesopore volume ( $V_{\text{meso}}$ ) and total pore volume ( $V_{\text{total}}$ ),  
 10 BET-specific surface area ( $S_{\text{BET}}$ ) and ash content of LAC.

Sample	$V_{\text{micro}} (<2\text{nm})$ $\text{cm}^3 \text{ g}^{-1}$	$V_{\text{meso}} (2 -50 \text{ nm})$ $\text{cm}^3 \text{ g}^{-1}$	$V_{\text{total}} \text{ cm}^3 \text{ g}^{-1}$	$S_{\text{BET}}$ $\text{m}^2 \text{ g}^{-1}$	Ash content (%)
LAC	0.40	0.12	0.57 ( $< 137 \text{ nm}$ )	$1367 \pm 1$	19

11  
 12  
 13 Finally, Figure 1c reported the thermogravimetric analysis of the LAC produced. The ash content  
 14 evaluated is reported in Table 2 and is about 19 %. This result may depend on the natural origin  
 15 of the raw material.

16  
 17 **3.2. Structural and Morphological Investigations**

1  
2  
3  
4  
5  
6  
7  
8  
9  
10  
11  
12  
13  
14  
15  
16  
17  
18  
19  
20  
21  
22  
23  
24  
25  
26  
27  
28  
29  
30  
31  
32  
33  
34  
35  
36  
37  
38  
39  
40  
41  
42  
43  
44  
45  
46  
47  
48  
49  
50  
51  
52  
53  
54  
55  
56  
57  
58  
59  
60  
61  
62  
63  
64  
65

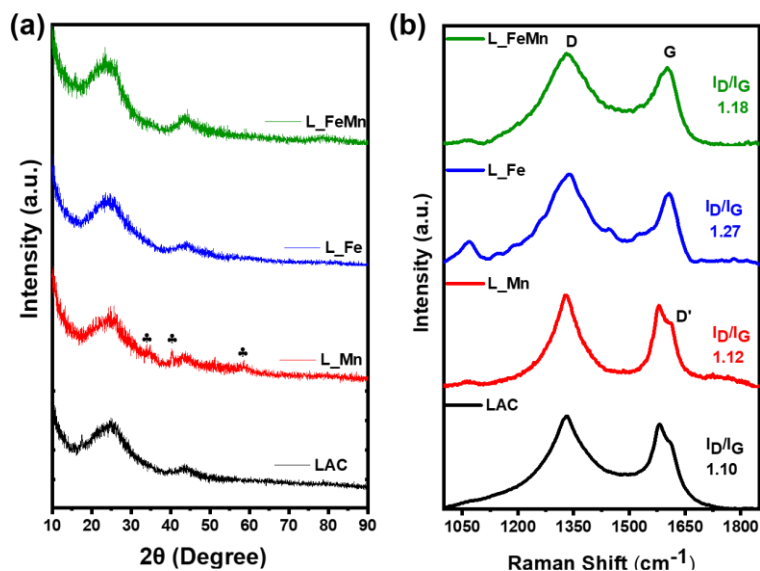


Figure 2. XRD patterns (a) and Raman spectra (b) of the as-developed samples.

Soon after the functionalization of the LAC with the MPC of interest, qualitative elemental analysis was carried out using XRF (Figure S1). Each sample showed clear peaks of the metal of interest i.e. Fe and/or Mn, justifying the effectiveness of the synthesis process. However, pristine LAC (Figure S1a) contained a few traces of Fe, Cu and Ni, which probably were present in the raw material or got introduced as contamination during the processing and therefore were minutely present in every sample. Since the relative presence of impurities was too low they were not considered contributors to ORR and were unheeded. Moreover, XRD was employed with the aim of phase identification and two broader peaks that emerged nearly at 25° and 43.5° were indexed to (002) and (101) planes of carbon, respectively, portending the distorted nature of the graphitic matrix [75,76] (Figure 2a). Only, sample L\_Mn demonstrated very tiny peaks of MnO at ~34.9°, ~40.5° and ~58°, consistent with JPDs# 01-089-4835. Kumar et al. also experienced such tiny MnO peaks in the XRD pattern of bimetallic ORR electrocatalysts fabricated by dual functionalization of carbon nanotubes with FePc and MnPc [40]. However, quite interestingly, L\_Fe and L\_FeMn demonstrated only the diffraction peaks of carbon, giving an impression of the homogenized distribution of Fe and Mn-based species in the carbon matrix without forming coarser crystalline nanoparticles [76–79]. In our case, the usage of MPC in a relatively smaller proportion might have restricted the excessive coalescence of metallic species into coarser nanoparticles. Moreover, appreciable prevention of metal nanoclustering up to a pyrolysis

1 temperature of 600 °C has already been witnessed [80]. The carbonaceous structure of the resultant  
2 electrocatalysts was further examined by the way of Raman spectroscopy as demonstrated in  
3 [Figure 2b](#). All the samples revealed typical G (nearly at 1590 cm<sup>-1</sup>) and D (nearly at 1330 cm<sup>-1</sup>)  
4 bands, due to in-plane stretching of the sp<sup>2</sup> carbon atom with E<sub>2g</sub> symmetry and breathing mode of  
5 A<sub>1g</sub> symmetry, respectively [81,82]. LAC and L\_Mn also exhibited a D' band in the vicinity of  
6 1613 cm<sup>-1</sup>. The G band is conventionally ascribed to graphitization content while the D and D'  
7 band emerges because of the structural disruption and induced defects in the original lattice [81–  
8 85]. It is worth mentioning that every sample had a higher D peak indicating a greater extent of  
9 disorders and defects in the carbon architecture, which could substantially participate in enhancing  
10 the ORR activity due to modified electronic and chemical characteristics of the disrupted carbons  
11 [76,86,87]. As it is well known, the ratio of D to G band intensity (I<sub>D</sub>/I<sub>G</sub>) manifests the degree of  
12 disorder in carbon-based materials. I<sub>D</sub>/I<sub>G</sub> remained always higher than unity where this intensity  
13 ratio reached the maximum value of 1.27 for L\_Fe followed by 1.18 for L\_FeMn which indicates  
14 the occurrence of a very high defect density.

### 3.3. Surface Chemistry and Morphology

17 It was shown that the surface chemistry of the electrocatalysts plays a crucial role in the  
18 electrocatalytic activity and the mechanisms that are taking place [88,89]. Therefore, XPS was  
19 used to identify the surface composition. The acquired full survey scans provided in [Figure S2](#)  
20 indicate the prevalence of carbon, nitrogen and oxygen as major constituents where silicon is  
21 present as an impurity element. In the metal functionalized samples i.e. L\_Mn, L\_Fe and L\_FeMn  
22 tiny peaks belonging to Mn and/or Fe can be appreciated while the high-resolution 2p spectra of  
23 Mn and Fe in the corresponding samples are additionally displayed in [Figure S3](#). The intensities  
24 of both Mn2p and Fe2p spectra came out to be very low and thus agreed with the XRD findings,  
25 suggesting the homogenous presence of metallic content in traces. Li and coworkers also  
26 experienced such kind of structure while developing trace bimetallic ORR electrocatalysts [51].  
27 [Table S1](#) summarizes the elemental composition as well as the relative proportion of the nitrogen-  
28 based species present in the samples.

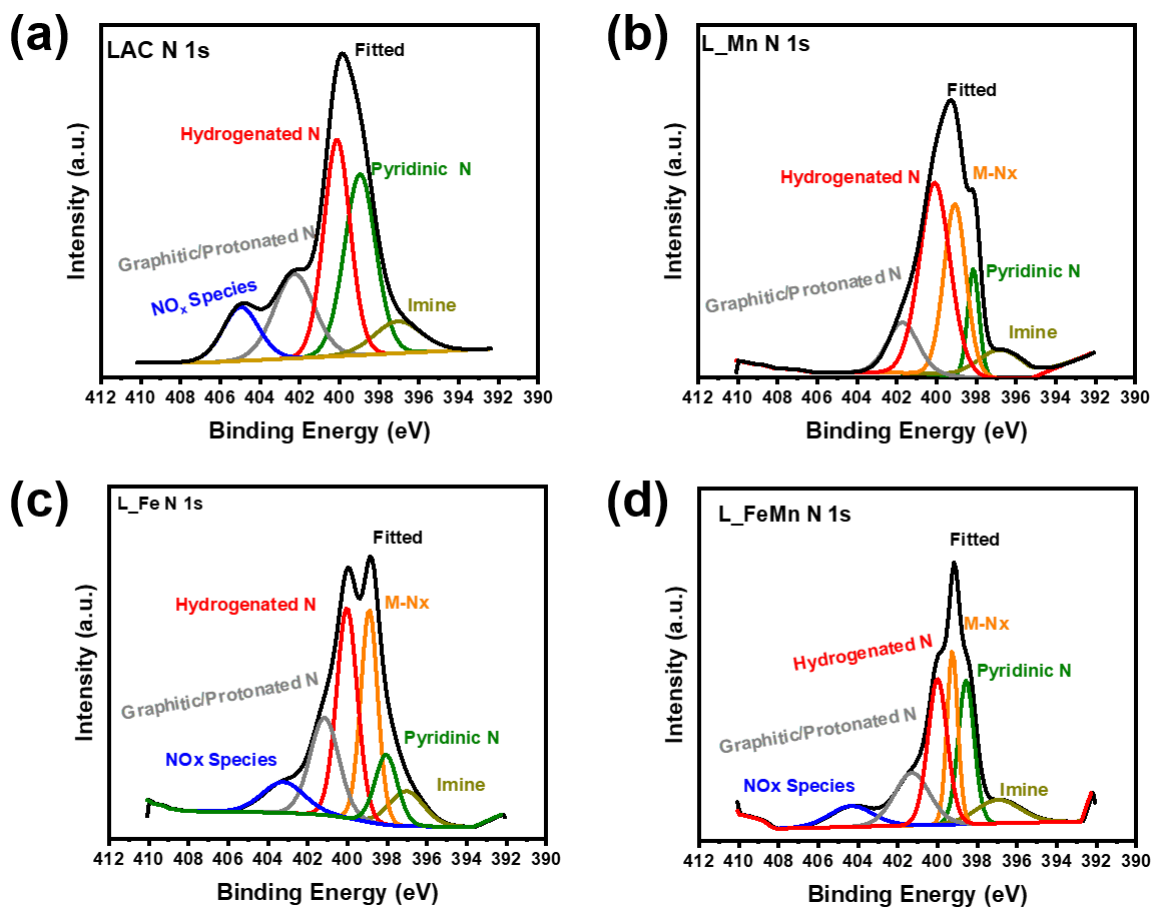
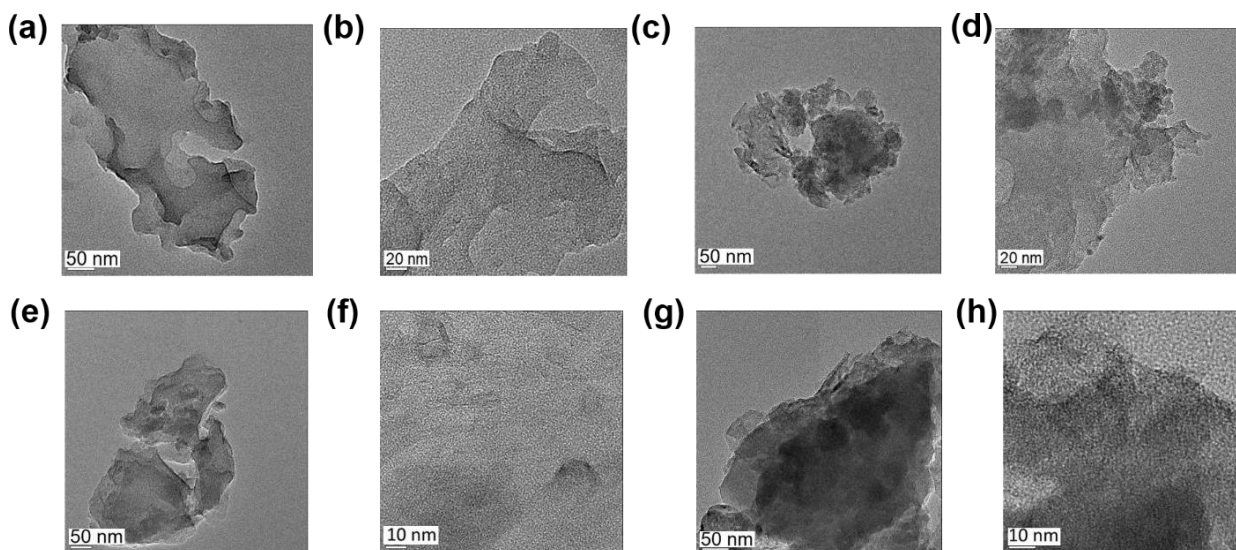


Figure 3. XPS high-resolution N 1s spectra of the as-developed samples.

As afore discussed in detail, nitrogen is an important ingredient of M-N-Cs and helps in specifying the route of ORR, N 1s high-resolution spectra of the derived samples (Figure 3) were thoroughly analyzed. Deconvolution of N 1s peak of LAC indicated the occurrence of various nitrogen species such as imine N, pyridinic N, hydrogenated N, graphitic/protonated N, and NO<sub>x</sub>, emerging in the vicinity of their typical binding energies [21,90–95]. Interestingly the metal functionalized sample also demonstrated the presence of M-N<sub>x</sub>. Whereas pyridinic N (0.5 at.%) was maximum in LAC with a total nitrogen content of 1.87 at.%. Nitrogen came out to be the highest in L\_Fe (3.4 at.%) with the predominance of M-N<sub>x</sub>, hydrogenated N-H and graphitic N whereas pyridinic N remained 0.36-38 at.% in all three metal functionalized samples. It is worth mentioning that the co-occurrence of various active sites can be advantageous since each of them performs particular tasks during ORR [52]. Generally, pyridinic N is considered essential for completing the electro-reduction of oxygen, especially as a secondary active site [21]. However,

1 Okada et al. also experienced superior activity of graphitic N owing to lower defect density [96].  
2 Lai et al experienced the dependency of limiting current density on graphitic N while pyridine N  
3 predicted the onset potential [97]. On the other hand, Kabir et al. revealed that hydrogenated N  
4 (including pyrrolic and Pyridinic N-H) not only uplifts the reaction kinetics but also acts as key  
5 active sites for the 2+2 e- transfer mechanism ORR in both alkaline and acidic media while  
6 pyridinic N being secondary active site can be helpful in further reducing the peroxide in the  
7 alkaline environment [94]. In addition to metal-free nitrogen-based moieties, M-N<sub>x</sub> is expected to  
8 carry out the direct tetra-electronic reduction of oxygen into water [98]. Moreover, the reactivity  
9 of such active sites is also governed by the nature of the electrolyte to which they are exposed and  
10 their roles alter as the pH of the electrolyte changes [35]. Shifting from acidic to alkaline conditions  
11 switches pyridinic N-H to deprotonated pyridinic N<sup>-</sup> which is a preferential adsorption site for O<sub>2</sub>  
12 due to enhanced Lewis basicity [35,99].



13 **Figure 4.** TEM images of LAC (a, b), L\_Mn (c, d), L\_Fe (e, f) and L\_FeMn (g, h).

14  
15  
16 The morphological features of the derived samples were studied by the means of TEM.  
17 Obtained micrographs are illustrated in [Figure 4](#). LAC demonstrated a well-developed porous  
18 structure. Such aspects of the microstructure were sustained in the MPC functionalized samples as  
19 well. Microstructural features could be relatable to the outcomes of Raman spectroscopy and XRD  
20 that highlighted the presence of structural defects and disorders. In a high-resolution image of  
21 L\_Fe ([Figure 4f](#)) a few broken graphitic domains could be appreciated. Interestingly, TEM  
22 micrographs of functionalized electrocatalysts didn't show substantial agglomeration or

1  
2  
3  
4 1 nanoparticle formation of metallic species which further validates the impression of atomically  
5  
6 2 dispersed metallic moieties in a homogenous fashion [100]. EDS presented in Figure S4 further  
7  
8 3 confirms the elements of interest i.e. Fe and Mn in the corresponding samples whereas peaks of  
9  
10 4 Cu belong to the TEM sample holder and Si is an impurity artifact.  
11  
12 5

### 13 6 **3.4 Electrochemical Activity**

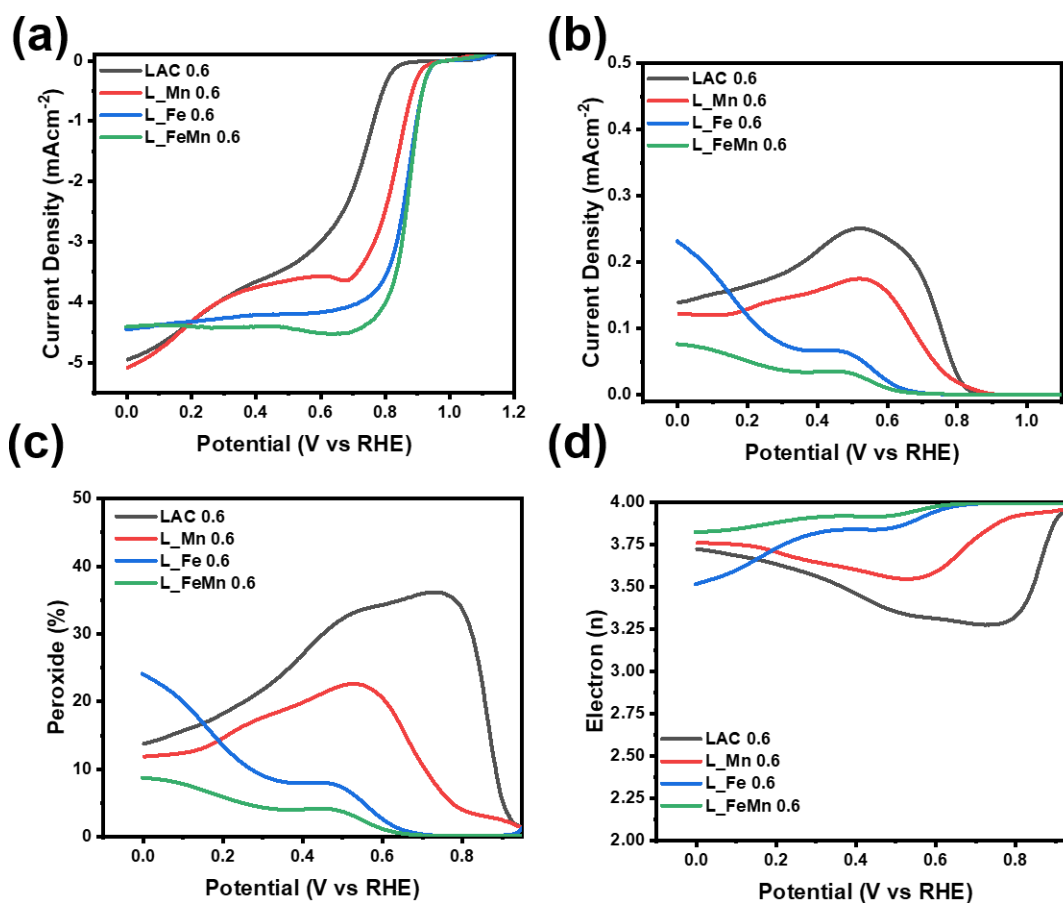
14  
15 7 To elucidate the electrocatalytic aptitude of the developed electrocatalysts, RRDE measurements  
16  
17 8 were carried out. Changing the nature of working electrolytes not only modifies the reaction  
18  
19 9 mechanism but different active sites respond to ORR activity differently [101,102]. For that  
20  
21 10 reason, ORR measurements were obtained in alkaline and acidic media, to ensure the utility of the  
22  
23 11 developed electrocatalyst for AEMFC and PEMFCs, respectively. Onset potential ( $E_{\text{onset}}$ ), half-  
24  
25 12 wave potential ( $E_{1/2}$ ) and limiting current density ( $I_{\text{limit}}$ ) are the common performance indicator  
26  
27 13 acquired from RRDE while the electrocatalyst loading on the disk of RRDE may affect the  
28  
29 14 peroxide formation. Therefore, two different loadings of  $0.2 \text{ mg cm}^{-2}$  and  $0.6 \text{ mg cm}^{-2}$  were  
30  
31 15 individually utilized to analyze the electrochemical aspects of the studied electrocatalysts.  
32  
33 16

#### 34 17 **3.3.1 ORR Performance in Alkaline Media**

35 18 Figure 5 demonstrates the ORR activity in  $\text{O}_2$ -saturated  $0.1 \text{ M KOH}$  with electrocatalysts loading  
36  
37 19 of  $0.6 \text{ mg cm}^{-2}$  while the performance with one-third loading is additionally presented in  
38  
39 20 Supplementary Figure S5. Polarization curves attained at a  $5 \text{ mV s}^{-1}$  scan rate highlighted the active  
40  
41 21 nature of the developed electrocatalysts, however, the pristine LAC came out to be the least  
42  
43 22 efficient with a higher overpotential. Remarkably, the functionalization of LAC with MPc  
44  
45 23 categorically improved the kinetics. Among all the counterparts, L\_Fe and L\_FeMn exhibited the  
46  
47 24 highest  $E_{\text{onset}}$  of  $\sim 0.94 \text{ V}$  (vs RHE) with an outstanding  $E_{1/2}$  of  $0.87 \text{ V}$  (vs RHE).  $I_{\text{limit}}$  remained  
48  
49 25 maximum for L\_FeMn. LAC and L\_Mn showed  $E_{1/2}$  of  $\sim 0.75 \text{ V}$  (vs RHE) and  $0.85 \text{ V}$  (vs RHE)  
50  
51 26 respectively, with  $0.6 \text{ mg cm}^{-2}$  catalyst loadings. Peroxide production showed interesting trends  
52  
53 27 where the electrocatalyst loading also contributed to diminishing the yield of unwanted  $\text{OH}_2^-$ . A  
54  
55 28 threefold increment in the electrocatalyst loading resulted in a slight positive shift of the  $E_{1/2}$  along  
56  
57 29 with a subsequent drop in the peroxide yield. Actually, with higher loading, the produced peroxide  
58  
59 30 gets scavenged and then reduced within the denser layer of the electrocatalyst [103–106]. LAC  
60  
61 31 and L\_Mn initially came out to be peroxide-producing electrocatalysts at lower overpotential  
62  
63  
64  
65



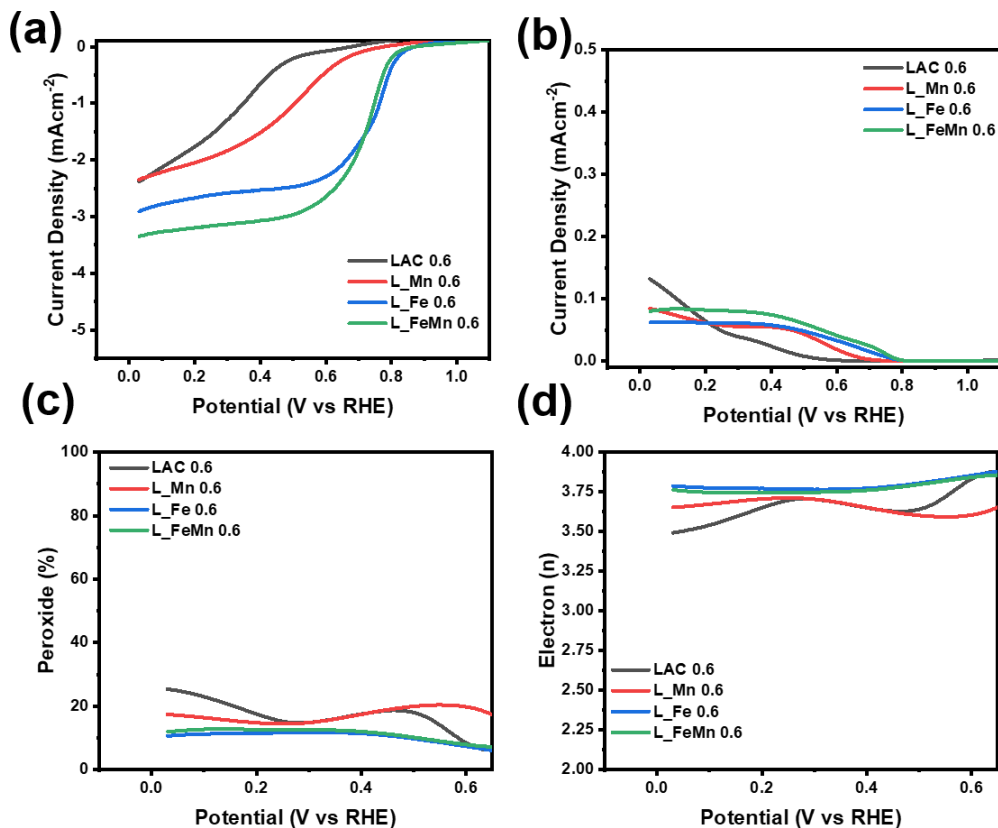
1 however a definite decline in the peroxide production can be seen as the applied potential increases.  
 2 This speculation endorses the probability of a 2+2 electrons reduction pathway where the  
 3 generated peroxide is afterward reduced at the secondary sites. On the other hand, L\_Fe and  
 4 L\_FeMn tended to restrict the peroxide formation in a nearly tetra-electronic fashion. In the case  
 5 of L\_FeMn, peroxide yield remained confined to a maximum of ~16% and 8.7% while the electron  
 6 transfer number was above 3.68 and 3.83 with 0.2 and 0.6 mg cm<sup>-2</sup> loading, respectively. Overall  
 7 superior electrocatalytic activity is essentially credited to the dual-doping of Fe and Mn due to  
 8 which electro-reduction of oxygen was synergistically boosted [40,50–52].



10  
 11 **Figure 5.** RRDE measurements of the developed electrocatalysts in O<sub>2</sub>-saturated 0.1 M KOH at  
 12 1600 rpm with electrocatalyst loading of 0.6 mg cm<sup>-2</sup>. ORR LSVs obtained at 5 mV s<sup>-1</sup> (a), ring  
 13 current densities (b), peroxide yield (c) and the number of electrons (d) transferred during ORR.

### 15 3.3.2 ORR Performance in Acid Media

1 The efficacy of the developed electrocatalysts was additionally probed in acidic conditions  
 2 comprising O<sub>2</sub>-rich 0.5 M H<sub>2</sub>SO<sub>4</sub>, again using two different loadings of 0.6 mg cm<sup>-2</sup> (Figure 6) and  
 3 0.2 mg cm<sup>-2</sup> (Figure S6). In acidic conditions, L\_Fe with 0.6 mg cm<sup>-2</sup> loading exhibited E<sub>onset</sub> and  
 4 E<sub>1/2</sub> at 0.84 V (vs RHE) and 0.77 V (vs RHE), respectively, while the I<sub>limit</sub> came out to be relatively  
 5 lower. Whereas L\_FeMn with an E<sub>onset</sub> of 0.82 V (vs RHE) showed the highest I<sub>limit</sub>. Again L\_Mn  
 6 demonstrated the least activity among the MPC functionalized samples, confirming the  
 7 inevitability of Fe for carrying out ORR with superior kinetics. Electron transfer number and  
 8 peroxide yield remained nearly the same for both L\_Fe and L\_FeMn. Both yielded peroxide ~11-  
 9 12% while maintaining the nearly tetra-electronic pathway where the electrons transfer came out  
 10 to be above 3.75. Similar to alkaline situations, a positive influence of electrocatalyst loading on  
 11 the ORR performance was observed and again higher loading not only improved the kinetics but  
 12 also effectively decreased the peroxide yield.



14  
 15 **Figure 6.** RRDE measurements of the developed electrocatalysts in O<sub>2</sub>-saturated 0.5 M H<sub>2</sub>SO<sub>4</sub>  
 16 at 1600 rpm with electrocatalyst loading of 0.6 mg cm<sup>-2</sup>. ORR LSVs obtained at 5 mV s<sup>-1</sup> (a),

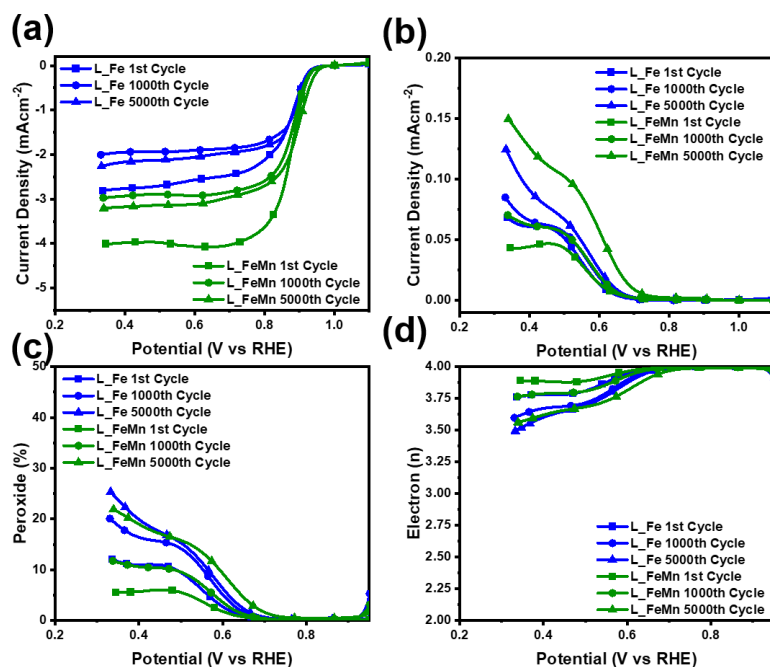
1  
2  
3  
4 1 ring current densities (b), peroxide yield (c) and the number of electrons (d) transferred during  
5  
6 2 ORR  
7  
8 3

### 4 3.3.3 Electrochemical stability

11  
12 5 Overall electrocatalytic activity of the L\_Fe and L\_FeMn turn out to be comparable where  
13  
14 6 L\_FeMn exhibited relatively lower peroxide yield, particularly in alkaline media. While  
15  
16 7 comparing different sorts of monometallic and bimetallic M-N-Cs, Lilloja et al. also experienced  
17  
18 8 the best performance exhibited by Fe-containing monometallic and FeMn bimetallic  
19  
20 9 electrocatalysts [52]. Electrocatalytic activity of L\_Fe and L\_FeMn could be attributed to  
21  
22 10 structural defects as revealed by Raman, porous carbonaceous architecture visible in TEM  
23  
24 11 micrograph along with the coexistence of different nitrogen moieties confirmed by XPS.  
25  
26 12 Furthermore, microstructural analysis negated the possible agglomeration or nanoparticle  
27  
28 13 formation of metallic species in both samples and endorsed the homogeneous distribution at the  
29  
30 14 atomic level. Moreover, lower production of peroxide with satisfactory kinetics of L\_FeMn can  
31  
32 15 be accredited to the synergic effect of Fe and Mn [40,41,50–52].

33 16 Along with favorable kinetics and desired selectivity, operational durability is an essential criterion  
34  
35 17 to be fulfilled by the electrocatalysts. For this reason, accelerated stability tests for L\_Fe and  
36  
37 18 L\_FeMn have been performed over 5000 continuous cycles at 50 mV s<sup>-1</sup>. From **Figure 7**, in an  
38  
39 19 alkaline environment, reasonable stability of E<sub>1/2</sub> for both electrocatalysts can be acknowledged,  
40  
41 20 however, a negative shift in I<sub>limit</sub> can be clearly seen. At the potential of 0.4 V, I<sub>limit</sub> of L\_Fe was  
42  
43 21 diminished by 0.59 mA cm<sup>-2</sup> while I<sub>limit</sub> of L\_FeMn was lowered from 3.97 to 3.17 mA cm<sup>-2</sup> by  
44  
45 22 the 5000<sup>th</sup> cycle but still remained categorically higher than that of L\_Fe. The obvious impact of  
46  
47 23 this observation can be speculated on the peroxide yield and the number of electrons transferred  
48  
49 24 during ORR. In the case of L\_Fe, peroxide production was increased from 10.1% to 20.12%  
50  
51 25 whereas in L\_FeMn the undesirable increment in peroxide was restricted to 18.5% at 0.4 V.  
52  
53 26 However, both electrocatalysts demonstrated nearly tetra-electronic reduction of oxygen where  
54  
55 27 electron transfer number persisted above 3.5. Overall, the durability aspects of both  
56  
57 28 electrocatalysts remained more or less the same however, L\_FeMn demonstrated a relatively  
58  
59 29 higher I<sub>limit</sub> and slightly lesser uplift in the yield of peroxide over continuous cycling. The  
60  
61 30 satisfactory robustness of L\_FeMn encouraged the execution of stability measurements  
62  
63 31 additionally in the acidic conditions i.e. O<sub>2</sub>-saturated 0.5 M H<sub>2</sub>SO<sub>4</sub> and achieved trends are  
64  
65

1 illustrated in Figure S7. In the acidic electrolyte, the electrocatalyst didn't exhibit appreciable  
 2 durability where both  $E_{1/2}$  and  $I_{limit}$  were considerably affected as the cycles proceeded. By the end  
 3 of the stability test, L\_FeMn was left with insufficient electrocatalytic activity. The instability of  
 4 PGM-free electrocatalysts in electrocatalytic media is known and there could be various complex  
 5 factors damaging the durability including demetalation, deterioration of active moieties, carbon  
 6 oxidation and so on [107,108]. However, analyzing the exact mechanism behind the limited  
 7 stability in acidic conditions is somehow beyond the scope of the current study.



8  
 9 **Figure 7.** Illustrates the stability trends of the 5000 cycles in O<sub>2</sub>-saturated 0.1 M KOH with 0.6  
 10 mg cm<sup>-2</sup> loading of L\_Fe and L\_FeMn on RRDE. ORR LSVs obtained at 5 mV s<sup>-1</sup> (a), ring  
 11 current densities (b), peroxide yield (c) and the number of electrons (d) transferred during ORR  
 12

#### 13 4. Fuel Cell Testing

14  
15  
16  
17  
18  
19  
20  
21  
22  
23  
24  
25  
26  
27  
28  
29  
30  
31  
32  
33  
34  
35  
36  
37  
38  
39  
40  
41  
42  
43  
44  
45  
46  
47  
48  
49  
50  
51  
52  
53  
54  
55  
56  
57  
58  
59  
60  
61  
62  
63  
64  
65

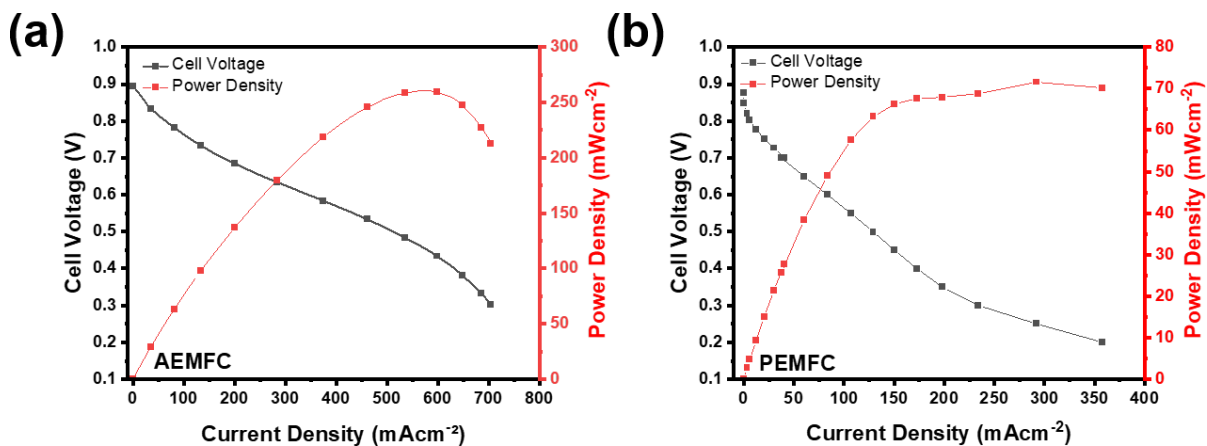


Figure 8. Full device characterization using L\_FeMn as cathode electrocatalyst to perform ORR in (a) AEMFC and (b) PEMFC.

Owing to appreciable electro-kinetics and stability demonstrated by L\_FeMn during the RRDE measurements, the sample was finally configured as a cathode catalyst to perform ORR in the running FCs. Full device characterizations were implemented to affirm the practicality of L\_FeMn for cathode applications in both AEMFC and PEMFC. From Figure 8a, the performance of AEMFC configured with L\_FeMn containing cathode can be acknowledged. AEMFC operating with a feed of pure O<sub>2</sub> (0.6 L min<sup>-1</sup>) at 60 °C delivered an open circuit voltage (OCV) of 0.893 V. A peak power density (P<sub>max</sub>) of 261 mW cm<sup>-2</sup> was observed at the current density of ~577 mA cm<sup>-2</sup>. On the other hand, when L\_FeMn was integrated as an ORR electrocatalyst in the cathodic configuration of PEMFC the performance was not as good as that of AEMFC, indicating that these electrocatalysts can be better employed in the alkaline environment rather than acidic environment. PEMFC was assembled with NR-211 Nafion membrane where the air was fed at the cathode operating at 80 °C. As can be seen in Figure 8b, PEMFC exhibited OCV of 0.88 V with P<sub>max</sub> of ~72 mW cm<sup>-2</sup> at the current density of ~292 mA cm<sup>-2</sup>.

Reasonable outcomes in AEMFC are consistent with the outstanding ORR activity of L\_FeMn in the alkaline media during the half-cell testing, confirming the utility of waste biomass-derived electrocatalysts for FC applications. In spite of the fact that a true comparison with previously reported results is a bit difficult task due to variations in the designing parameters of materials and operating conditions [109–111], the obtained AEMFC performance with L\_FeMn is comparable to some earlier reports. Very recently, Teppor and coworkers utilized decomposed peat as a carbon

1 precursor for synthesizing PGM-free ORR electrocatalyst and obtained  $P_{\max}$  of  $51 \text{ mW cm}^{-2}$  when  
2 deployed as a cathode catalyst in AEMFC [112]. Not long ago, Lilloja et al. reported Fe–N–C  
3 electrocatalyst prepared using VariPore™ method by Pajarito Powder which demonstrated  $P_{\max}$  of  
4  $220 \text{ mW cm}^{-2}$  when applied in AEMFC containing HMT-PMBI membrane [113]. Similarly, Hao  
5 et al. prepared multiple metals and heteroatom self-doped biomass-derived electrocatalyst which  
6 performed outstandingly during the half-cell analyses in both acidic and alkaline media, however,  
7 while used as an air-breathing PEMFC cathode it delivered  $17.6 \text{ mW cm}^{-2}$  with an OCV of 0.966  
8 V [114]. Moreover, by the virtue of high-temperature pyrolysis, Lilloja et al. produced various  
9 monometallic and bimetallic M-N-C for ORR activity in AEMFCs. They observed identical  
10 behavior of monometallic Fe-N-MPC and bimetallic FeMn-N-MPC during the RRDE  
11 measurements together with outstanding  $P_{\max}$  of 473 and  $474 \text{ mW cm}^{-2}$ , respectively, in AEMFC.  
12 Although our full device performances are still inferior to what could be obtained using state-of-  
13 the-art electrocatalysts as indicated in the literature [110,115–123], the usage of waste biomass for  
14 the fabrication of cost-effective and efficient electrocatalysts presents a novel pathway under the  
15 framework of the circular economy. Despite the promising performance of advanced ORR  
16 electrocatalysts, their realistic employment for mass-scale FC applications is limited due to the  
17 involvement of the high cost and synthetic complexity of carbon-based materials i.e. carbon  
18 nanotubes and graphene-based materials [124]. Whereas the pyrolysis of largely available waste  
19 biomass not only provides a sustainable alternative for the cost-effective development of carbon-  
20 based electrocatalysts for green energy storage applications but also presents an effective strategy  
21 for waste recycling and environmental safety.

## 22 23 **5. Conclusion**

24 Lignin, being waste biomass of negligible economical worth, was used to first produce activated  
25 char containing networked porosity. Afterward, it was functionalized with FePc and MnPc through  
26 a simplistic pyrolysis process in order to fabricate monometallic and bimetallic electrocatalysts.  
27 The developed electrocatalysts demonstrated defect-rich porous structures without any  
28 substitutional agglomeration in the form of metallic nanoparticles. XPS confirmed the presence of  
29 a variety of nitrogen-containing active moieties. RRDE measurements in both alkaline and acidic  
30 media with two different loading of  $0.2 \text{ mg cm}^{-2}$  and  $0.6 \text{ mg cm}^{-2}$  validated the active nature of the  
31 derived electrocatalysts. In alkaline media, L\_Fe and L\_FeMn showed outstanding  $E_{\text{onset}}$  of  $\sim 0.942$

1  
2  
3  
4 1 V together with an  $E_{1/2}$  of 0.874 V which surpasses the kinetic attributes shown by the benchmark  
5  
6 2 Pt/C electrocatalysts. L\_FeMn showed decidedly lower peroxide yield with a clear tetra-electronic  
7  
8 3 electro-reduction of  $O_2$  in 0.1 M KOH and also qualified for operational stability. Electrocatalytic  
9  
10 4 performance L\_Fe can be linked to the favorable morphological attributes and coexistence of  
11  
12 5 desired nitrogen moieties. While the subsequent reduction in peroxide yield could be additionally  
13  
14 6 attributed synergistic of Fe and Mn. On the other hand, under acidic conditions, L\_FeMn had a  
15  
16 7 slightly lower  $E_{onset}$  (0.817 V) than that of L\_Fe (0.837 V). Contrary to 0.1 M KOH, the durability  
17  
18 8 of L\_FeMn was severely affected in 0.5M  $H_2SO_4$  over the 5000 cycles. Finally, to affirm the  
19  
20 9 realistic utility of L\_FeMn for ORR in FCs it was configured as cathode electrocatalysts in both  
21  
22 10 PEMFC and AEMFC which delivered  $P_{max}$  of  $\sim 72 \text{ mW cm}^{-2}$  (at  $292 \text{ mA cm}^{-2}$ ) and  $261 \text{ mW cm}^{-2}$   
23  
24 11 (at  $\sim 577 \text{ mA cm}^{-2}$ ), respectively. Last but not the least, this works signposts the new avenues for  
25  
26 12 the cost-effective development of waste-derived M-N-Cs for lethargic ORR in a circular way.  
27  
28 13

## 28 14 **Acknowledgments**

29  
30  
31 15 C.S. would like to thank the support from the Italian Ministry of Education, Universities and  
32  
33 16 Research (Ministero dell'Istruzione, dell'Università e della Ricerca – MIUR) through the “Rita  
34  
35 17 Levi Montalcini 2018” fellowship (Grant number PGR18MAZLI). The authors also thank the  
36  
37 18 Italian ministry MIUR for funding through the FISR 2019 project AMPERE (FISR2019\_01294).  
38  
39 19 University of Bologna authors acknowledge MUR support under the project “ECOSYSTEM FOR  
40  
41 20 SUSTAINABLE TRANSITION IN EMILIA-ROMAGNA” of the National Recovery and  
42  
43 21 Resilience Plan (NRRP)  
44

## 45 22 **References**

- 46  
47 23  
48  
49 24 [1] H. Zhang, H. Osgood, X. Xie, Y. Shao, G. Wu, Engineering nanostructures of PGM-free oxygen-  
50 25 reduction catalysts using metal-organic frameworks, *Nano Energy*. 31 (2017) 331–350.  
51 26 <https://doi.org/10.1016/j.nanoen.2016.11.033>.  
52 27 [2] M.K. Debe, Electrocatalyst approaches and challenges for automotive fuel cells, *Nature*. 486 (2012)  
53 28 43–51. <https://doi.org/10.1038/nature11115>.  
54 29 [3] Y. He, S. Liu, C. Priest, Q. Shi, G. Wu, Atomically dispersed metal–nitrogen–carbon catalysts for  
55 30 fuel cells: advances in catalyst design, electrode performance, and durability improvement, *Chem.*  
56 31 *Soc. Rev.* 49 (2020) 3484–3524. <https://doi.org/10.1039/C9CS00903E>.  
57 32 [4] N. Ramaswamy, S. Mukerjee, Fundamental Mechanistic Understanding of Electrocatalysis of  
58 33 Oxygen Reduction on Pt and Non-Pt Surfaces: Acid versus Alkaline Media, *Advances in Physical*  
59 34 *Chemistry*. 2012 (2012). <https://doi.org/10.1155/2012/491604>.  
60  
61  
62  
63  
64  
65

- 1  
2  
3  
4 1 [5] Y. Nie, L. Li, Z. Wei, Recent advancements in Pt and Pt-free catalysts for oxygen reduction  
5 2 reaction, *Chem. Soc. Rev.* 44 (2015) 2168–2201. <https://doi.org/10.1039/C4CS00484A>.  
6 3 [6] R. Ma, G. Lin, Y. Zhou, Q. Liu, T. Zhang, G. Shan, M. Yang, J. Wang, A review of oxygen  
7 4 reduction mechanisms for metal-free carbon-based electrocatalysts, *Npj Comput Mater.* 5 (2019) 1–  
8 5 15. <https://doi.org/10.1038/s41524-019-0210-3>.  
9 6 [7] A. Muthukrishnan, Y. Nabaie, T. Ohsaka, Role of iron in the reduction of H<sub>2</sub>O<sub>2</sub> intermediate during  
10 7 the oxygen reduction reaction on iron-containing polyimide-based electrocatalysts, *RSC Adv.* 6  
11 8 (2016) 3774–3777. <https://doi.org/10.1039/C5RA23162K>.  
12 9 [8] X. Zhao, Y. Liu, Origin of Selective Production of Hydrogen Peroxide by Electrochemical Oxygen  
13 10 Reduction, *J. Am. Chem. Soc.* 143 (2021) 9423–9428. <https://doi.org/10.1021/jacs.1c02186>.  
14 11 [9] J. Huang, Q. Lu, X. Ma, X. Yang, Bio-inspired FeN<sub>5</sub> moieties anchored on a three-dimensional  
15 12 graphene aerogel to improve oxygen reduction catalytic performance, *J. Mater. Chem. A.* 6 (2018)  
16 13 18488–18497. <https://doi.org/10.1039/C8TA06455E>.  
17 14 [10] S. Guo, S. Zhang, S. Sun, Tuning Nanoparticle Catalysis for the Oxygen Reduction Reaction,  
18 15 *Angewandte Chemie International Edition.* 52 (2013) 8526–8544.  
19 16 <https://doi.org/10.1002/anie.201207186>.  
20 17 [11] U. Tylus, Q. Jia, H. Hafiz, R.J. Allen, B. Barbiellini, A. Bansil, S. Mukerjee, Engendering anion  
21 18 immunity in oxygen consuming cathodes based on Fe-N<sub>x</sub> electrocatalysts: Spectroscopic and  
22 19 electrochemical advanced characterizations, *Applied Catalysis B: Environmental.* 198 (2016) 318–  
23 20 324. <https://doi.org/10.1016/j.apcatb.2016.05.054>.  
24 21 [12] Y. He, Q. Tan, L. Lu, J. Sokolowski, G. Wu, Metal-Nitrogen-Carbon Catalysts for Oxygen  
25 22 Reduction in PEM Fuel Cells: Self-Template Synthesis Approach to Enhancing Catalytic Activity  
26 23 and Stability, *Electrochemical Energy Reviews.* 2 (2019). <https://doi.org/10.1007/s41918-019-00031-9>.  
27 24 [13] S. Specchia, P. Atanassov, J.H. Zagal, Mapping transition metal–nitrogen–carbon  
28 25 catalyst performance on the critical descriptor diagram, *Current Opinion in Electrochemistry.* 27  
29 26 (2021) 100687. <https://doi.org/10.1016/j.coelec.2021.100687>.  
30 27 [14] M. Shen, C. Wei, K. Ai, L. Lu, Transition metal–nitrogen–carbon nanostructured catalysts for the  
31 28 oxygen reduction reaction: From mechanistic insights to structural optimization, *Nano Res.* 10  
32 29 (2017) 1449–1470. <https://doi.org/10.1007/s12274-016-1400-7>.  
33 30 [15] M.-X. Chen, L. Tong, H.-W. Liang, Understanding the Catalytic Sites of Metal–Nitrogen–Carbon  
34 31 Oxygen Reduction Electrocatalysts, *Chemistry – A European Journal.* 27 (2021) 145–157.  
35 32 <https://doi.org/10.1002/chem.202002427>.  
36 33 [16] K. Singh, F. (Sanaz) Razmjooei, J.-S. Yu, Active sites and factors influencing them for efficient  
37 34 oxygen reduction reaction in metal-N coordinated pyrolyzed and non-pyrolyzed catalysts: A review,  
38 35 *J. Mater. Chem. A.* 5 (2017). <https://doi.org/10.1039/C7TA05222G>.  
39 36 [17] C. Liu, H. Li, F. Liu, J. Chen, Z. Yu, Z. Yuan, C. Wang, H. Zheng, G. Henkelman, L. Wei, Y. Chen,  
40 37 Intrinsic Activity of Metal Centers in Metal–Nitrogen–Carbon Single-Atom Catalysts for Hydrogen  
41 38 Peroxide Synthesis, *J. Am. Chem. Soc.* 142 (2020) 21861–21871.  
42 39 <https://doi.org/10.1021/jacs.0c10636>.  
43 40 [18] P. Trogadas, T. Fuller, P. Strasser, Carbon as catalyst and support for electrochemical energy  
44 41 conversion, *Carbon.* 75 (2014) 5–42. <https://doi.org/10.1016/j.carbon.2014.04.005>.  
45 42 [19] D. Yan, Y. Li, J. Huo, R. Chen, L. Dai, S. Wang, Defect Chemistry of Nonprecious-Metal  
46 43 Electrocatalysts for Oxygen Reactions, *Advanced Materials.* 29 (2017) 1606459.  
47 44 <https://doi.org/10.1002/adma.201606459>.  
48 45 [20] J. He, T. Zheng, D. Wu, S. Zhang, M. Gu, Q. He, Insights into the Determining Effect of Carbon  
49 46 Support Properties on Anchoring Active Sites in Fe–N–C Catalysts toward the Oxygen Reduction  
50 47 Reaction, *ACS Catal.* 12 (2022) 1601–1613. <https://doi.org/10.1021/acscatal.1c04815>.  
51 48 [21] L. Yang, J. Shui, L. Du, Y. Shao, J. Liu, L. Dai, Z. Hu, Carbon-Based Metal-Free ORR  
52 49 Electrocatalysts for Fuel Cells: Past, Present, and Future, *Advanced Materials.* 31 (2019) 1804799.  
53 50 <https://doi.org/10.1002/adma.201804799>.  
54 51  
55  
56  
57  
58  
59  
60  
61  
62  
63  
64  
65



- 1  
2  
3  
4 1 [22] O.L. Li, K. Prabakar, A. Kaneko, H. Park, T. Ishizaki, Exploration of Lewis basicity and oxygen  
5 2 reduction reaction activity in plasma-tailored nitrogen-doped carbon electrocatalysts, *Catalysis*  
6 3 *Today*. 337 (2019). <https://doi.org/10.1016/j.cattod.2019.02.058>.  
7 4 [23] E. Berretti, M. Longhi, P. Atanassov, D. Sebastián, C. Lo Vecchio, V. Baglio, A. Serov, A.  
8 5 Marchionni, F. Vizza, C. Santoro, A. Lavacchi, Platinum group metal-free Fe-based (FeNC) oxygen  
9 6 reduction electrocatalysts for direct alcohol fuel cells, *Current Opinion in Electrochemistry*. 29  
10 7 (2021) 100756. <https://doi.org/10.1016/j.coelec.2021.100756>.  
11 8 [24] C.Z. Loyola, S. Ureta-Zañartu, J.H. Zagal, F. Tasca, Activity volcano plots for the oxygen reduction  
12 9 reaction using FeN<sub>4</sub> complexes: From reported experimental data to the electrochemical meaning,  
13 10 *Current Opinion in Electrochemistry*. 32 (2022) 100923.  
14 11 <https://doi.org/10.1016/j.coelec.2021.100923>.  
15 12 [25] K. Ozoemena, Nanostructured platinum-free electrocatalysts in alkaline direct alcohol fuel cells:  
16 13 Catalyst design, principles and applications, *RSC Adv.* 6 (2016).  
17 14 <https://doi.org/10.1039/C6RA15057H>.  
18 15 [26] J.H. Zagal, I. Ponce, R. Oñate, Redox Potentials as Reactivity Descriptors in Electrochemistry,  
19 16 IntechOpen, 2019. <https://doi.org/10.5772/intechopen.89883>.  
20 17 [27] U. Tylus, Q. Jia, K. Strickland, N. Ramaswamy, A. Serov, P. Atanassov, S. Mukerjee, Elucidating  
21 18 Oxygen Reduction Active Sites in Pyrolyzed Metal–Nitrogen Coordinated Non-Precious-Metal  
22 19 Electrocatalyst Systems, *J. Phys. Chem. C*. 118 (2014) 8999–9008.  
23 20 <https://doi.org/10.1021/jp500781v>.  
24 21 [28] R. Venegas, F.J. Recio, J. Riquelme, K. Neira, J.F. Marco, I. Ponce, J.H. Zagal, F. Tasca,  
25 22 Biomimetic reduction of O<sub>2</sub> in an acid medium on iron phthalocyanines axially coordinated to  
26 23 pyridine anchored on carbon nanotubes, *J. Mater. Chem. A*. 5 (2017) 12054–12059.  
27 24 <https://doi.org/10.1039/C7TA02381B>.  
28 25 [29] A. Kozhushner, N. Zion, L. Elbaz, Methods for assessment and measurement of the active site  
29 26 density in platinum group metal–free oxygen reduction reaction catalysts, *Current Opinion in*  
30 27 *Electrochemistry*. 25 (2021) 100620. <https://doi.org/10.1016/j.coelec.2020.08.002>.  
31 28 [30] Q. Jia, N. Ramaswamy, U. Tylus, K. Strickland, J. Li, A. Serov, K. Artyushkova, P. Atanassov, J.  
32 29 Anibal, C. Gumeci, S.C. Barton, M.-T. Sougrati, F. Jaouen, B. Halevi, S. Mukerjee, Spectroscopic  
33 30 insights into the nature of active sites in iron–nitrogen–carbon electrocatalysts for oxygen reduction  
34 31 in acid, *Nano Energy*. 29 (2016) 65–82. <https://doi.org/10.1016/j.nanoen.2016.03.025>.  
35 32 [31] J.H. Zagal, S. Griveau, J.F. Silva, T. Nyokong, F. Bedioui, Metallophthalocyanine-based molecular  
36 33 materials as catalysts for electrochemical reactions, *Coordination Chemistry Reviews*. 254 (2010)  
37 34 2755–2791. <https://doi.org/10.1016/j.ccr.2010.05.001>.  
38 35 [32] J. Zagal, M. Páez, A.A. Tanaka, J.R. dos Santos, C.A. Linkous, Electrocatalytic activity of metal  
39 36 phthalocyanines for oxygen reduction, *Journal of Electroanalytical Chemistry*. 339 (1992) 13–30.  
40 37 [https://doi.org/10.1016/0022-0728\(92\)80442-7](https://doi.org/10.1016/0022-0728(92)80442-7).  
41 38 [33] T. Marshall-Roth, N.J. Libretto, A.T. Wrobel, K.J. Anderton, M.L. Pegis, N.D. Ricke, T.V. Voorhis,  
42 39 J.T. Miller, Y. Surendranath, A pyridinic Fe–N<sub>4</sub> macrocycle models the active sites in Fe/N-doped  
43 40 carbon electrocatalysts, *Nat Commun*. 11 (2020) 5283. [https://doi.org/10.1038/s41467-020-18969-](https://doi.org/10.1038/s41467-020-18969-6)  
44 41 [6](https://doi.org/10.1038/s41467-020-18969-6).  
45 42 [34] X.X. Wang, M.T. Swihart, G. Wu, Achievements, challenges and perspectives on cathode catalysts  
46 43 in proton exchange membrane fuel cells for transportation, *Nat Catal*. 2 (2019) 578–589.  
47 44 <https://doi.org/10.1038/s41929-019-0304-9>.  
48 45 [35] T. Asset, P. Atanassov, Iron-Nitrogen-Carbon Catalysts for Proton Exchange Membrane Fuel Cells,  
49 46 *Joule*. 4 (2020) 33–44. <https://doi.org/10.1016/j.joule.2019.12.002>.  
50 47 [36] U. Martinez, S. Komini Babu, E.F. Holby, H.T. Chung, X. Yin, P. Zelenay, Progress in the  
51 48 Development of Fe-Based PGM-Free Electrocatalysts for the Oxygen Reduction Reaction,  
52 49 *Advanced Materials*. 31 (2019) 1806545. <https://doi.org/10.1002/adma.201806545>.  
53 50 [37] Q. Liu, Y. Wang, Z. Hu, Z. Zhang, Iron-based single-atom electrocatalysts: synthetic strategies and  
54 51 applications, *RSC Adv.* 11 (2021) 3079–3095. <https://doi.org/10.1039/D0RA08223F>.  
55  
56  
57  
58  
59  
60  
61  
62  
63  
64  
65

- 1  
2  
3  
4 1 [38] J. Li, M.T. Sougrati, A. Zitolo, J.M. Ablett, I.C. Oğuz, T. Mineva, I. Matanovic, P. Atanassov, Y.  
5 2 Huang, I. Zenyuk, A. Di Cicco, K. Kumar, L. Dubau, F. Maillard, G. Dražić, F. Jaouen,  
6 3 Identification of durable and non-durable Fe<sub>Nx</sub> sites in Fe–N–C materials for proton exchange  
7 4 membrane fuel cells, *Nat Catal.* 4 (2021) 10–19. <https://doi.org/10.1038/s41929-020-00545-2>.
- 8 5 [39] W. Wang, Q. Jia, S. Mukerjee, S. Chen, Recent Insights into the Oxygen-Reduction Electrocatalysis  
9 6 of Fe/N/C Materials, *ACS Catal.* 9 (2019) 10126–10141. <https://doi.org/10.1021/acscatal.9b02583>.
- 10 7 [40] Y. Kumar, E. Kibena-Pöldsepp, J. Kozlova, M. Rähn, A. Treshchalov, A. Kikas, V. Kisand, J.  
11 8 Aruväli, A. Tamm, J.C. Douglin, S.J. Folkman, I. Gelmetti, F.A. Garcés-Pineda, J.R. Galán-  
12 9 Mascarós, D.R. Dekel, K. Tammeveski, Bifunctional Oxygen Electrocatalysis on Mixed Metal  
13 10 Phthalocyanine-Modified Carbon Nanotubes Prepared via Pyrolysis, *ACS Appl. Mater. Interfaces.*  
14 11 13 (2021) 41507–41516. <https://doi.org/10.1021/acsami.1c06737>.
- 15 12 [41] A. Serov, M.H. Robson, M. Smolnik, P. Atanassov, Templated bi-metallic non-PGM catalysts for  
16 13 oxygen reduction, *Electrochimica Acta.* 80 (2012) 213–218.  
17 14 <https://doi.org/10.1016/j.electacta.2012.07.008>.
- 18 15 [42] B. Zhong, L. Zhang, J. Yu, K. Fan, Ultrafine iron-cobalt nanoparticles embedded in nitrogen-doped  
19 16 porous carbon matrix for oxygen reduction reaction and zinc-air batteries, *Journal of Colloid and*  
20 17 *Interface Science.* 546 (2019) 113–121. <https://doi.org/10.1016/j.jcis.2019.03.038>.
- 21 18 [43] W. Ran, J. Dong, T. Sun, J. Chen, L. Xu, Iron, Cobalt, and Nitrogen Tri-Doped Ordered  
22 19 Mesoporous Carbon as a Highly Efficient Electrocatalyst for Oxygen Reduction Reaction,  
23 20 *ChemistrySelect.* 4 (2019) 7728–7733. <https://doi.org/10.1002/slct.201901641>.
- 24 21 [44] W.-K. Jo, S. Moru, D.-E. Lee, S. Tonda, Cobalt- and iron-coordinated graphitic carbon nitride on  
25 22 reduced graphene oxide: A nonprecious bimetallic M–N<sub>x</sub>–C analogue electrocatalyst for efficient  
26 23 oxygen reduction reaction in acidic media, *Applied Surface Science.* 531 (2020) 147367.  
27 24 <https://doi.org/10.1016/j.apsusc.2020.147367>.
- 28 25 [45] Z. Hu, Z. Guo, Z. Zhang, M. Dou, F. Wang, Bimetal Zeolitic Imidazolate Framework-Derived Iron-,  
29 26 Cobalt- and Nitrogen-Codoped Carbon Nanopolyhedra Electrocatalyst for Efficient Oxygen  
30 27 Reduction, *ACS Appl. Mater. Interfaces.* 10 (2018) 12651–12658.  
31 28 <https://doi.org/10.1021/acsami.8b00512>.
- 32 29 [46] R. Mercado, C. Wahl, J. En Lu, T. Zhang, B. Lu, P. Zhang, J.Q. Lu, A. Allen, J.Z. Zhang, S. Chen,  
33 30 Nitrogen-Doped Porous Carbon Cages for Electrocatalytic Reduction of Oxygen: Enhanced  
34 31 Performance with Iron and Cobalt Dual Metal Centers, *ChemCatChem.* 12 (2020) 3230–3239.  
35 32 <https://doi.org/10.1002/cctc.201902324>.
- 36 33 [47] Priorities for critical materials for a circular economy, EASAC – the European Academies’ Science  
37 34 Advisory Council, Halle (Saale) Germany, 2016.
- 38 35 [48] I. Directorate-General for Internal Market, S. Bobba, P. Claudiu, D. Huygens, P. Alves Dias, B.  
39 36 Gawlik, E. Tzimas, D. Wittmer, P. Nuss, M. Grohol, H. Saveyn, F. Buraoui, G. Orveillon, T.  
40 37 Hámor, S. Slavko, F. Mathieux, M. Gislev, C. Torres De Matos, G.A. Blengini, F. Ardente, D.  
41 38 Blagoeva, E. Garbarino, Report on critical raw materials and the circular economy, Publications  
42 39 Office of the European Union, LU, 2018. <https://data.europa.eu/doi/10.2873/167813> (accessed May  
43 40 7, 2022).
- 44 41 [49] Y. Sun, L. Silvioli, N.R. Sahraie, W. Ju, J. Li, A. Zitolo, S. Li, A. Bagger, L. Arnarson, X. Wang, T.  
45 42 Moeller, D. Bernsmeier, J. Rossmesl, F. Jaouen, P. Strasser, Activity–Selectivity Trends in the  
46 43 Electrochemical Production of Hydrogen Peroxide over Single-Site Metal–Nitrogen–Carbon  
47 44 Catalysts, *J. Am. Chem. Soc.* 141 (2019) 12372–12381. <https://doi.org/10.1021/jacs.9b05576>.
- 48 45 [50] M. Kodali, C. Santoro, S. Herrera, A. Serov, P. Atanassov, Bimetallic platinum group metal-free  
49 46 catalysts for high power generating microbial fuel cells, *Journal of Power Sources.* 366 (2017) 18–  
50 47 26. <https://doi.org/10.1016/j.jpowsour.2017.08.110>.
- 51 48 [51] F. Li, P. Shi, J. Wu, X. Qi, Y. Liu, G. Li, Trace Bimetallic Iron/Manganese Co-Doped N-  
52 49 Ketjenblack Carbon Electrocatalyst for Robust Oxygen Reduction Reaction, *J. Electrochem. Soc.*  
53 50 168 (2021) 060502. <https://doi.org/10.1149/1945-7111/ac03f3>.
- 54  
55  
56  
57  
58  
59  
60  
61  
62  
63  
64  
65

- 1  
2  
3  
4 1 [52] J. Lilloja, E. Kibena-Pöldsepp, A. Sarapuu, M. Käärrik, J. Kozlova, P. Paiste, A. Kikas, A.  
5 2 Treshchalov, J. Leis, A. Tamm, V. Kisand, S. Holdcroft, K. Tammeveski, Transition metal and  
6 3 nitrogen-doped mesoporous carbons as cathode catalysts for anion-exchange membrane fuel cells,  
7 4 *Applied Catalysis B: Environmental*. 306 (2022) 121113.  
8 5 <https://doi.org/10.1016/j.apcatb.2022.121113>.  
9 6 [53] M. Borghei, J. Lehtonen, L. Liu, O.J. Rojas, *Advanced Biomass-Derived Electrocatalysts for the*  
10 7 *Oxygen Reduction Reaction*, *Advanced Materials*. 30 (2018) 1703691.  
11 8 <https://doi.org/10.1002/adma.201703691>.  
12 9 [54] M. Wang, S. Wang, H. Yang, W. Ku, S. Yang, Z. Liu, G. Lu, Carbon-Based Electrocatalysts  
13 10 Derived From Biomass for Oxygen Reduction Reaction: A Minireview, *Frontiers in Chemistry*. 8  
14 11 (2020). <https://www.frontiersin.org/article/10.3389/fchem.2020.00116> (accessed May 7, 2022).  
15 12 [55] L. Du, G. Zhang, X. Liu, A. Hassanpour, M. Dubois, A.C. Tavares, S. Sun, Biomass-derived  
16 13 nonprecious metal catalysts for oxygen reduction reaction: The demand-oriented engineering of  
17 14 active sites and structures, *Carbon Energy*. 2 (2020) 561–581. <https://doi.org/10.1002/cey2.73>.  
18 15 [56] M. Jiang, X. Yu, H. Yang, S. Chen, Optimization Strategies of Preparation of Biomass-Derived  
19 16 Carbon Electrocatalyst for Boosting Oxygen Reduction Reaction: A Minireview, *Catalysts*. 10  
20 17 (2020) 1472. <https://doi.org/10.3390/catal10121472>.  
21 18 [57] S. Zago, M. Bartoli, M. Muhyuddin, G.M. Vanacore, P. Jagdale, A. Tagliaferro, C. Santoro, S.  
22 19 Specchia, Engineered biochar derived from pyrolyzed waste tea as a carbon support for Fe-N-C  
23 20 electrocatalysts for the oxygen reduction reaction, *Electrochimica Acta*. 412 (2022) 140128.  
24 21 <https://doi.org/10.1016/j.electacta.2022.140128>.  
25 22 [58] J. Munuera, L. Britnell, C. Santoro, R. Cuéllar-Franca, C. Casiraghi, A review on sustainable  
26 23 production of graphene and related life cycle assessment, *2D Mater*. 9 (2021) 012002.  
27 24 <https://doi.org/10.1088/2053-1583/ac3f23>.  
28 25 [59] B.K. Mutuma, N.F. Sylla, A. Bubu, N.M. Ndiaye, C. Santoro, A. Brilloni, F. Poli, N. Manyala, F.  
29 26 Soavi, Valorization of biodigester plant waste in electrodes for supercapacitors and microbial fuel  
30 27 cells, *Electrochimica Acta*. 391 (2021) 138960. <https://doi.org/10.1016/j.electacta.2021.138960>.  
31 28 [60] M. Muhyuddin, P. Mustarelli, C. Santoro, Recent Advances in Waste Plastic Transformation into  
32 29 Valuable Platinum-Group Metal-Free Electrocatalysts for Oxygen Reduction Reaction,  
33 30 *ChemSusChem*. 14 (2021) 3785–3800. <https://doi.org/10.1002/cssc.202101252>.  
34 31 [61] N. Cai, H. Yang, X. Zhang, S. Xia, D. Yao, P. Bartocci, F. Fantozzi, Y. Chen, H. Chen, P.T.  
35 32 Williams, Bimetallic carbon nanotube encapsulated Fe-Ni catalysts from fast pyrolysis of waste  
36 33 plastics and their oxygen reduction properties, *Waste Management*. 109 (2020) 119–126.  
37 34 <https://doi.org/10.1016/j.wasman.2020.05.003>.  
38 35 [62] N. Cai, S. Xia, X. Zhang, Z. Meng, P. Bartocci, F. Fantozzi, Y. Chen, H. Chen, P.T. Williams, H.  
39 36 Yang, Preparation of Iron- and Nitrogen-Codoped Carbon Nanotubes from Waste Plastics Pyrolysis  
40 37 for the Oxygen Reduction Reaction, *ChemSusChem*. 13 (2020) 938–944.  
41 38 <https://doi.org/10.1002/cssc.201903293>.  
42 39 [63] G. Daniel, T. Kosmala, M.C. Dalconi, L. Nodari, D. Badocco, P. Pastore, A. Lorenzetti, G.  
43 40 Granozzi, C. Durante, Upcycling of polyurethane into iron-nitrogen-carbon electrocatalysts active  
44 41 for oxygen reduction reaction, *Electrochimica Acta*. 362 (2020) 137200.  
45 42 <https://doi.org/10.1016/j.electacta.2020.137200>.  
46 43 [64] M. Muhyuddin, J. Filippi, L. Zoia, S. Bonizzoni, R. Lorenzi, E. Berretti, L. Capozzoli, M. Bellini,  
47 44 C. Ferrara, A. Lavacchi, C. Santoro, Waste Face Surgical Mask Transformation into Crude Oil and  
48 45 Nanostructured Electrocatalysts for Fuel Cells and Electrolyzers, *ChemSusChem*. 15 (2022)  
49 46 e202102351. <https://doi.org/10.1002/cssc.202102351>.  
50 47 [65] *Converting Waste Agricultural Biomass into a Resource-Compendium of Technologies*, United  
51 48 Nations Environmental Programme, , Japan, 2009.  
52 49 <https://wedocs.unep.org/xmlui/handle/20.500.11822/7614> (accessed May 7, 2022).  
53  
54  
55  
56  
57  
58  
59  
60  
61  
62  
63  
64  
65

- 1  
2  
3  
4 1 [66] H. Zhou, T. Fan, D. Zhang, Biotemplated Materials for Sustainable Energy and Environment:  
5 2 Current Status and Challenges, *ChemSusChem*. 4 (2011) 1344–1387.  
6 3 <https://doi.org/10.1002/cssc.201100048>.  
7 4 [67] D.L. Klass, *Biomass for Renewable Energy, Fuels, and Chemicals*, Elsevier, 1998.  
8 5 [68] M. Garedeew, F. Lin, B. Song, T.M. DeWinter, J.E. Jackson, C.M. Saffron, C.H. Lam, P.T. Anastas,  
9 6 Greener Routes to Biomass Waste Valorization: Lignin Transformation Through Electrocatalysis  
10 7 for Renewable Chemicals and Fuels Production, *ChemSusChem*. 13 (2020) 4214–4237.  
11 8 <https://doi.org/10.1002/cssc.202000987>.  
12 9 [69] H.Y. Lim, S. Yusup, A.C.M. Loy, S. Samsuri, S.S.K. Ho, A.S.A. Manaf, S.S. Lam, B.L.F. Chin,  
13 10 M.N. Acda, P. Unrean, E. Rianawati, Review on Conversion of Lignin Waste into Value-Added  
14 11 Resources in Tropical Countries, *Waste Biomass Valor.* 12 (2021) 5285–5302.  
15 12 <https://doi.org/10.1007/s12649-020-01307-8>.  
16 13 [70] D.S. Bajwa, G. Pourhashem, A.H. Ullah, S.G. Bajwa, A concise review of current lignin  
17 14 production, applications, products and their environmental impact, *Industrial Crops and Products*.  
18 15 139 (2019) 111526. <https://doi.org/10.1016/j.indcrop.2019.111526>.  
19 16 [71] I. Haq, P. Mazumder, A.S. Kalamdhad, Recent advances in removal of lignin from paper industry  
20 17 wastewater and its industrial applications – A review, *Bioresource Technology*. 312 (2020) 123636.  
21 18 <https://doi.org/10.1016/j.biortech.2020.123636>.  
22 19 [72] M. Bellini, M.V. Pagliaro, A. Lenarda, P. Fornasiero, M. Marelli, C. Evangelisti, M. Innocenti, Q.  
23 20 Jia, S. Mukerjee, J. Jankovic, L. Wang, J.R. Varcoe, C.B. Krishnamurthy, I. Grinberg, E. Davydova,  
24 21 D.R. Dekel, H.A. Miller, F. Vizza, Palladium–Ceria Catalysts with Enhanced Alkaline Hydrogen  
25 22 Oxidation Activity for Anion Exchange Membrane Fuel Cells, *ACS Appl. Energy Mater.* 2 (2019)  
26 23 4999–5008. <https://doi.org/10.1021/acsaem.9b00657>.  
27 24 [73] H.A. Miller, M.V. Pagliaro, M. Bellini, F. Bartoli, L. Wang, I. Salam, J.R. Varcoe, F. Vizza,  
28 25 Integration of a Pd-CeO<sub>2</sub>/C Anode with Pt and Pt-Free Cathode Catalysts in High Power Density  
29 26 Anion Exchange Membrane Fuel Cells, *ACS Appl. Energy Mater.* 3 (2020) 10209–10214.  
30 27 <https://doi.org/10.1021/acsaem.0c01998>.  
31 28 [74] L. Wang, X. Peng, W.E. Mustain, J.R. Varcoe, Radiation-grafted anion-exchange membranes: the  
32 29 switch from low- to high-density polyethylene leads to remarkably enhanced fuel cell performance,  
33 30 *Energy Environ. Sci.* 12 (2019) 1575–1579. <https://doi.org/10.1039/C9EE00331B>.  
34 31 [75] S. Liu, L. Liu, X. Chen, Z. Yang, M. Li, Y. Wang, W. Lv, P. Zhu, X. Zhao, G. Wang, On an Easy  
35 32 Way to Prepare Fe, S, N Tri-Doped Mesoporous Carbon Materials as Efficient Electrocatalysts for  
36 33 Oxygen Reduction Reaction, *Electrocatalysis*. 10 (2019) 72–81. <https://doi.org/10.1007/s12678-018-0496-9>.  
37 34 [76] C. Zhu, Q. Shi, B. Xu, S. Fu, G. Wan, C. Yang, S. Yao, J. Song, H. Zhou, D. Du, S. Beckman, D.  
38 35 Su, Y. Lin, Hierarchically Porous M-N-C (M = Co and Fe) Single-Atom Electrocatalysts with  
39 36 Robust MN x Active Moieties Enable Enhanced ORR Performance, *Advanced Energy Materials*. 8  
40 37 (2018) 1801956. <https://doi.org/10.1002/aenm.201801956>.  
41 38 [77] T. Liu, F. Sun, M. Huang, L. Guan, Atomically dispersed Co–N–C electrocatalysts synthesized by a  
42 39 low-speed ball milling method for proton exchange membrane fuel cells, *Materials Advances*. 3  
43 40 (2022) 1565–1573. <https://doi.org/10.1039/D1MA00809A>.  
44 41 [78] X. Luo, X. Wei, H. Wang, W. Gu, T. Kaneko, Y. Yoshida, X. Zhao, C. Zhu, Secondary-Atom-  
45 42 Doping Enables Robust Fe–N–C Single-Atom Catalysts with Enhanced Oxygen Reduction  
46 43 Reaction, *Nano-Micro Lett.* 12 (2020) 163. <https://doi.org/10.1007/s40820-020-00502-5>.  
47 44 [79] C. Xin, W. Shang, J. Hu, C. Zhu, J. Guo, J. Zhang, H. Dong, W. Liu, Y. Shi, Integration of  
48 45 Morphology and Electronic Structure Modulation on Atomic Iron- Nitrogen- Carbon Catalysts for  
49 46 Highly Efficient Oxygen Reduction, *Advanced Functional Materials*. 32 (2022).  
50 47 <https://doi.org/10.1002/adfm.202108345>.  
51 48 [80] H. Yang, L. Shang, Q. Zhang, R. Shi, G. Waterhouse, L. Gu, T. Zhang, A universal ligand mediated  
52 49 method for large scale synthesis of transition metal single atom catalysts, *Nature Communications*.  
53 50 10 (2019) 1–9. <https://doi.org/10.1038/s41467-019-12510-0>.  
54 51  
55  
56  
57  
58  
59  
60  
61  
62  
63  
64  
65

- 1  
2  
3  
4 1 [81] A.C. Ferrari, J. Robertson, Interpretation of Raman spectra of disordered and amorphous carbon,  
5 2 Phys. Rev. B. 61 (2000) 14095–14107. <https://doi.org/10.1103/PhysRevB.61.14095>.
- 6 3 [82] L.G. Cançado, A. Jorio, E.H.M. Ferreira, F. Stavale, C.A. Achete, R.B. Capaz, M.V.O. Moutinho,  
7 4 A. Lombardo, T.S. Kulmala, A.C. Ferrari, Quantifying Defects in Graphene via Raman  
8 5 Spectroscopy at Different Excitation Energies, Nano Lett. 11 (2011) 3190–3196.  
9 6 <https://doi.org/10.1021/nl201432g>.
- 10 7 [83] C. Casimero, C. Hegarty, R.J. McGlynn, J. Davis, Ultrasonic exfoliation of carbon fiber:  
11 8 electroanalytical perspectives, J Appl Electrochem. 50 (2020) 383–394.  
12 9 <https://doi.org/10.1007/s10800-019-01379-y>.
- 13 10 [84] B.J. Matsoso, K. Ranganathan, B.K. Mutuma, T. Lerotholi, G. Jones, N.J. Coville, Time-dependent  
14 11 evolution of the nitrogen configurations in N-doped graphene films, RSC Adv. 6 (2016) 106914–  
15 12 106920. <https://doi.org/10.1039/C6RA24094A>.
- 16 13 [85] L.M. Malard, M.A. Pimenta, G. Dresselhaus, M.S. Dresselhaus, Raman spectroscopy in graphene,  
17 14 Physics Reports. 473 (2009) 51–87. <https://doi.org/10.1016/j.physrep.2009.02.003>.
- 18 15 [86] P. Song, M. Luo, X. Liu, W. Xing, W. Xu, Z. Jiang, L. Gu, Zn Single Atom Catalyst for Highly  
19 16 Efficient Oxygen Reduction Reaction, Advanced Functional Materials. 27 (2017) 1700802.  
20 17 <https://doi.org/10.1002/adfm.201700802>.
- 21 18 [87] J. Wang, F. Ciucci, Boosting Bifunctional Oxygen Electrolysis for N-Doped Carbon via Bimetal  
22 19 Addition, Small. 13 (2017) 1604103. <https://doi.org/10.1002/smll.201604103>.
- 23 20 [88] K. Artyushkova, A. Serov, S. Rojas-Carbonell, P. Atanassov, Chemistry of Multitudinous Active  
24 21 Sites for Oxygen Reduction Reaction in Transition Metal–Nitrogen–Carbon Electrocatalysts, J.  
25 22 Phys. Chem. C. 119 (2015) 25917–25928. <https://doi.org/10.1021/acs.jpcc.5b07653>.
- 26 23 [89] C. Santoro, P. Bollella, B. Erable, P. Atanassov, D. Pant, Oxygen reduction reaction electrocatalysis  
27 24 in neutral media for bioelectrochemical systems, Nat Catal. 5 (2022) 473–484.  
28 25 <https://doi.org/10.1038/s41929-022-00787-2>.
- 29 26 [90] P. Lazar, R. Mach, M. Otyepka, Spectroscopic Fingerprints of Graphitic, Pyrrolic, Pyridinic, and  
30 27 Chemisorbed Nitrogen in N-Doped Graphene, J. Phys. Chem. C. 123 (2019) 10695–10702.  
31 28 <https://doi.org/10.1021/acs.jpcc.9b02163>.
- 32 29 [91] K. Artyushkova, Misconceptions in interpretation of nitrogen chemistry from x-ray  
33 30 photoelectron spectra, Journal of Vacuum Science & Technology A. 38 (2020) 031002.  
34 31 <https://doi.org/10.1116/1.5135923>.
- 35 32 [92] M. Kodali, C. Santoro, A. Serov, S. Kabir, K. Artyushkova, I. Matanovic, P. Atanassov, Air  
36 33 Breathing Cathodes for Microbial Fuel Cell using Mn-, Fe-, Co- and Ni-containing Platinum Group  
37 34 Metal-free Catalysts, Electrochimica Acta. 231 (2017) 115–124.  
38 35 <https://doi.org/10.1016/j.electacta.2017.02.033>.
- 39 36 [93] M.J. Dzara, K. Artyushkova, S. Shulda, M.B. Strand, C. Ngo, E.J. Crumlin, T. Gennett, S.  
40 37 Pylypenko, Characterization of Complex Interactions at the Gas–Solid Interface with in Situ  
41 38 Spectroscopy: The Case of Nitrogen-Functionalized Carbon, J. Phys. Chem. C. 123 (2019) 9074–  
42 39 9086. <https://doi.org/10.1021/acs.jpcc.9b00487>.
- 43 40 [94] S. Kabir, K. Artyushkova, A. Serov, P. Atanassov, Role of Nitrogen Moieties in N-Doped 3D-  
44 41 Graphene Nanosheets for Oxygen Electroreduction in Acidic and Alkaline Media, ACS Appl.  
45 42 Mater. Interfaces. 10 (2018) 11623–11632. <https://doi.org/10.1021/acsami.7b18651>.
- 46 43 [95] C. Santoro, S. Rojas-Carbonell, R. Awais, R. Gokhale, M. Kodali, A. Serov, K. Artyushkova, P.  
47 44 Atanassov, Influence of platinum group metal-free catalyst synthesis on microbial fuel cell  
48 45 performance, Journal of Power Sources. 375 (2018) 11–20.  
49 46 <https://doi.org/10.1016/j.jpowsour.2017.11.039>.
- 50 47 [96] T. Okada, K.Y. Inoue, G. Kalita, M. Tanemura, T. Matsue, M. Meyyappan, S. Samukawa, Bonding  
51 48 state and defects of nitrogen-doped graphene in oxygen reduction reaction, Chemical Physics  
52 49 Letters. 665 (2016) 117–120. <https://doi.org/10.1016/j.cplett.2016.10.061>.
- 53  
54  
55  
56  
57  
58  
59  
60  
61  
62  
63  
64  
65

- 1  
2  
3  
4 1 [97] L. Lai, J.R. Potts, D. Zhan, L. Wang, C.K. Poh, C. Tang, H. Gong, Z. Shen, J. Lin, R.S. Ruoff,  
5 2 Exploration of the active center structure of nitrogen-doped graphene-based catalysts for oxygen  
6 3 reduction reaction, *Energy Environ. Sci.* 5 (2012) 7936–7942. <https://doi.org/10.1039/C2EE21802J>.  
7 4 [98] I. Matanovic, K. Artyushkova, P. Atanassov, Understanding PGM-free catalysts by linking density  
8 5 functional theory calculations and structural analysis: Perspectives and challenges, *Current Opinion*  
9 6 *in Electrochemistry.* 9 (2018) 137–144. <https://doi.org/10.1016/j.coelec.2018.03.009>.  
10 7 [99] S. Rojas-Carbonell, K. Artyushkova, A. Serov, C. Santoro, I. Matanovic, P. Atanassov, Effect of pH  
11 8 on the Activity of Platinum Group Metal-Free Catalysts in Oxygen Reduction Reaction, *ACS Catal.*  
12 9 8 (2018) 3041–3053. <https://doi.org/10.1021/acscatal.7b03991>.  
13 10 [100] A. Serov, K. Artyushkova, P. Atanassov, Fe-N-C Oxygen Reduction Fuel Cell Catalyst Derived  
14 11 from Carbendazim: Synthesis, Structure, and Reactivity, *Advanced Energy Materials.* 4 (2014)  
15 12 1301735. <https://doi.org/10.1002/aenm.201301735>.  
16 13 [101] R. Sgarbi, K. Kumar, F. Jaouen, A. Zitolo, E.A. Ticianelli, F. Maillard, Oxygen reduction reaction  
17 14 mechanism and kinetics on M-N<sub>x</sub>Cy and M@N-C active sites present in model M-N-C catalysts  
18 15 under alkaline and acidic conditions, *J Solid State Electrochem.* 25 (2021) 45–56.  
19 16 <https://doi.org/10.1007/s10008-019-04436-w>.  
20 17 [102] W. Zhong, Z. Wang, S. Han, L. Deng, J. Yu, Y. Lin, X. Long, M. Gu, S. Yang, Identifying the  
21 18 Active Sites of a Single Atom Catalyst with pH-Universal Oxygen Reduction Reaction Activity,  
22 19 *Cell Reports Physical Science.* 1 (2020) 100115. <https://doi.org/10.1016/j.xcrp.2020.100115>.  
23 20 [103] S. Rojas-Carbonell, C. Santoro, A. Serov, P. Atanassov, Transition metal-nitrogen-carbon catalysts  
24 21 for oxygen reduction reaction in neutral electrolyte, *Electrochemistry Communications.* 75 (2017)  
25 22 38–42. <https://doi.org/10.1016/j.elecom.2016.12.011>.  
26 23 [104] D. Singh, J. Tian, K. Mamtani, J. King, J.T. Miller, U.S. Ozkan, A comparison of N-containing  
27 24 carbon nanostructures (CN<sub>x</sub>) and N-coordinated iron-carbon catalysts (FeNC) for the oxygen  
28 25 reduction reaction in acidic media, *Journal of Catalysis.* 317 (2014) 30–43.  
29 26 <https://doi.org/10.1016/j.jcat.2014.05.025>.  
30 27 [105] M. Muhyuddin, N. Zocche, R. Lorenzi, C. Ferrara, F. Poli, F. Soavi, C. Santoro, Valorization of the  
31 28 inedible pistachio shells into nanoscale transition metal and nitrogen codoped carbon-based  
32 29 electrocatalysts for hydrogen evolution reaction and oxygen reduction reaction, *Mater Renew*  
33 30 *Sustain Energy.* 11 (2022) 131–141. <https://doi.org/10.1007/s40243-022-00212-5>.  
34 31 [106] M. Muhyuddin, D. Testa, R. Lorenzi, G.M. Vanacore, F. Poli, F. Soavi, S. Specchia, W. Giurlani,  
35 32 M. Innocenti, L. Rosi, C. Santoro, Iron-based electrocatalysts derived from scrap tires for oxygen  
36 33 reduction reaction: Evolution of synthesis-structure-performance relationship in acidic, neutral and  
37 34 alkaline media, *Electrochimica Acta.* 433 (2022) 141254.  
38 35 <https://doi.org/10.1016/j.electacta.2022.141254>.  
39 36 [107] C.H. Choi, C. Baldizzone, J.-P. Grote, A.K. Schuppert, F. Jaouen, K.J.J. Mayrhofer, Stability of Fe-  
40 37 N-C Catalysts in Acidic Medium Studied by Operando Spectroscopy, *Angew Chem Int Ed Engl.* 54  
41 38 (2015) 12753–12757. <https://doi.org/10.1002/anie.201504903>.  
42 39 [108] Q. Ma, H. Jin, J. Zhu, Z. Li, H. Xu, B. Liu, Z. Zhang, J. Ma, S. Mu, Stabilizing Fe-N-C Catalysts as  
43 40 Model for Oxygen Reduction Reaction, *Advanced Science.* 8 (2021) 2102209.  
44 41 <https://doi.org/10.1002/advs.202102209>.  
45 42 [109] T.J. Omasta, L. Wang, X. Peng, C.A. Lewis, J.R. Varcoe, W.E. Mustain, Importance of balancing  
46 43 membrane and electrode water in anion exchange membrane fuel cells, *Journal of Power Sources.*  
47 44 375 (2018) 205–213. <https://doi.org/10.1016/j.jpowsour.2017.05.006>.  
48 45 [110] W.E. Mustain, Understanding how high-performance anion exchange membrane fuel cells were  
49 46 achieved: Component, interfacial, and cell-level factors, *Current Opinion in Electrochemistry.* 12  
50 47 (2018) 233–239. <https://doi.org/10.1016/j.coelec.2018.11.010>.  
51 48 [111] N. Ramaswamy, S. Mukerjee, Alkaline Anion-Exchange Membrane Fuel Cells: Challenges in  
52 49 Electrocatalysis and Interfacial Charge Transfer, *Chem. Rev.* 119 (2019) 11945–11979.  
53 50 <https://doi.org/10.1021/acs.chemrev.9b00157>.  
54  
55  
56  
57  
58  
59  
60  
61  
62  
63  
64  
65

- 1  
2  
3  
4 1 [112] P. Teppor, R. Jäger, M. Paalo, A. Adamson, M. Härmas, O. Volobujeva, J. Aruväli, R. Palm, E.  
5 2 Lust, Peat as a carbon source for non-platinum group metal oxygen electrocatalysts and AEMFC  
6 3 cathodes, *International Journal of Hydrogen Energy*. 47 (2022) 16908–16920.  
7 4 <https://doi.org/10.1016/j.ijhydene.2022.03.199>.  
8 5  
9 6 [113] J. Lilloja, M. Mooste, E. Kibena-Pöldsepp, A. Sarapuu, B. Zulevi, A. Kikas, H.-M. Piirsoo, A.  
10 7 Tamm, V. Kisand, S. Holdcroft, A. Serov, K. Tammeveski, Mesoporous iron-nitrogen co-doped  
11 8 carbon material as cathode catalyst for the anion exchange membrane fuel cell, *Journal of Power  
12 9 Sources Advances*. 8 (2021) 100052. <https://doi.org/10.1016/j.powera.2021.100052>.  
13 10  
14 11 [114] M. Hao, R. Dun, Y. Su, L. He, F. Ning, X. Zhou, W. Li, In situ self-doped biomass-derived porous  
15 12 carbon as an excellent oxygen reduction electrocatalyst for fuel cells and metal–air batteries, *J.  
16 13 Mater. Chem. A*. 9 (2021) 14331–14343. <https://doi.org/10.1039/D1TA01417J>.  
17 14  
18 15 [115] L. Wang, M. Bellini, H.A. Miller, J.R. Varcoe, A high conductivity ultrathin anion-exchange  
19 16 membrane with 500+ h alkali stability for use in alkaline membrane fuel cells that can achieve 2 W  
20 17 cm<sup>-2</sup> at 80 °C, *J. Mater. Chem. A*. 6 (2018) 15404–15412. <https://doi.org/10.1039/C8TA04783A>.  
21 18  
22 19 [116] P.G. Santori, F.D. Speck, S. Cherevko, H.A. Firouzjaie, X. Peng, W.E. Mustain, F. Jaouen, High  
23 20 Performance FeNC and Mn-oxide/FeNC Layers for AEMFC Cathodes, *J. Electrochem. Soc.* 167  
24 21 (2020) 134505. <https://doi.org/10.1149/1945-7111/abb7e0>.  
25 22  
26 23 [117] H. Adabi, A. Shakouri, N. Ul Hassan, J.R. Varcoe, B. Zulevi, A. Serov, J.R. Regalbuto, W.E.  
27 24 Mustain, High-performing commercial Fe–N–C cathode electrocatalyst for anion-exchange  
28 25 membrane fuel cells, *Nat Energy*. 6 (2021) 834–843. <https://doi.org/10.1038/s41560-021-00878-7>.  
29 26  
30 27 [118] Md.M. Hossen, Md.S. Hasan, Md.R.I. Sardar, J. bin Haider, Mottakin, K. Tammeveski, P.  
31 28 Atanassov, State-of-the-art and developmental trends in platinum group metal-free cathode catalyst  
32 29 for anion exchange membrane fuel cell (AEMFC), *Applied Catalysis B: Environmental*. (2022)  
33 30 121733. <https://doi.org/10.1016/j.apcatb.2022.121733>.  
34 31  
35 32 [119] X. Peng, V. Kashyap, B. Ng, S. Kurungot, L. Wang, J.R. Varcoe, W.E. Mustain, High-Performing  
36 33 PGM-Free AEMFC Cathodes from Carbon-Supported Cobalt Ferrite Nanoparticles, *Catalysts*. 9  
37 34 (2019) 264. <https://doi.org/10.3390/catal9030264>.  
38 35  
39 36 [120] H. Adabi, P.G. Santori, A. Shakouri, X. Peng, K. Yassin, I.G. Rasin, S. Brandon, D.R. Dekel, N.U.  
40 37 Hassan, M.-T. Sougrati, A. Zitolo, J.R. Varcoe, J.R. Regalbuto, F. Jaouen, W.E. Mustain,  
41 38 Understanding how single-atom site density drives the performance and durability of PGM-free Fe–  
42 39 N–C cathodes in anion exchange membrane fuel cells, *Materials Today Advances*. 12 (2021)  
43 40 100179. <https://doi.org/10.1016/j.mtadv.2021.100179>.  
44 41  
45 42 [121] J. Woo, S.Y. Yang, Y.J. Sa, W.-Y. Choi, M.-H. Lee, H.-W. Lee, T.J. Shin, T.-Y. Kim, S.H. Joo,  
46 43 Promoting Oxygen Reduction Reaction Activity of Fe–N/C Electrocatalysts by Silica-Coating-  
47 44 Mediated Synthesis for Anion-Exchange Membrane Fuel Cells, *Chem. Mater.* 30 (2018) 6684–  
48 45 6701. <https://doi.org/10.1021/acs.chemmater.8b02117>.  
49 46  
50 47 [122] Y. Yang, X. Xu, P. Sun, H. Xu, L. Yang, X. Zeng, Y. Huang, S. Wang, D. Cao, AgNPs@Fe-N-C  
51 48 oxygen reduction catalysts for anion exchange membrane fuel cells, *Nano Energy*. 100 (2022)  
52 49 107466. <https://doi.org/10.1016/j.nanoen.2022.107466>.  
53 50  
54 51 [123] W. Xu, D. Yoon, Y. Yang, Y. Xiong, H. Li, R. Zeng, D.A. Muller, H.D. Abruña, MOF-Derived  
55 52 Bimetallic Pd–Co Alkaline ORR Electrocatalysts, *ACS Appl. Mater. Interfaces*. 14 (2022) 44735–  
56 53 44744. <https://doi.org/10.1021/acsami.2c10074>.  
57 54  
58 55 [124] S. Das, S. Ghosh, T. Kuila, N.C. Murmu, A. Kundu, Biomass-Derived Advanced Carbon-Based  
59 56 Electrocatalysts for Oxygen Reduction Reaction, *Biomass*. 2 (2022) 155–177.  
60 57 <https://doi.org/10.3390/biomass2030010>.  
61 58  
62 59  
63 60  
64 61  
65 62